

## Isopycnal Eddy Stirring Dominates Thermohaline Mixing in the Upper Subpolar North Atlantic



### Key Points:

- We quantify diapycnal and isopycnal contributions to thermohaline mixing in the subpolar North Atlantic with microstructure observations
- Isopycnal stirring dominates thermohaline mixing suggesting a key role in the water-mass transformations driving the overturning circulation
- The relative importance of isopycnal stirring is tracer-dependent, controlled by the large-scale co-variability of the tracer with density

### Correspondence to:

B. Fernández Castro,  
b.fernandez-castro@soton.ac.uk

### Citation:

Fernández Castro, B., Fernández Román, D., Ferron, B., Fontela, M., Lherminier, P., Naveira Garabato, A., et al. (2024). Isopycnal eddy stirring dominates thermohaline mixing in the upper subpolar North Atlantic. *Journal of Geophysical Research: Oceans*, 129, e2023JC020817. <https://doi.org/10.1029/2023JC020817>

Received 14 DEC 2023  
Accepted 4 SEP 2024

### Author Contributions:

**Conceptualization:** Bieito Fernández Castro, Bruno Ferron, Alberto Naveira Garabato, Carl Spingys, Kurt Polzin  
**Data curation:** Bieito Fernández Castro, Daniel Fernández Román, Pascale Lherminier  
**Formal analysis:** Bieito Fernández Castro, Daniel Fernández Román  
**Funding acquisition:** Pascale Lherminier, Fiz F. Pérez, Antón Velo  
**Investigation:** Bieito Fernández Castro, Daniel Fernández Román, Marcos Fontela  
**Methodology:** Bieito Fernández Castro, Daniel Fernández Román, Bruno Ferron, Alberto Naveira Garabato  
**Project administration:** Pascale Lherminier, Fiz F. Pérez, Antón Velo  
**Validation:** Bruno Ferron, Kurt Polzin  
**Visualization:** Bieito Fernández Castro

**Bieito Fernández Castro**<sup>1</sup> , **Daniel Fernández Román**<sup>2</sup> , **Bruno Ferron**<sup>3</sup> , **Marcos Fontela**<sup>4</sup> , **Pascale Lherminier**<sup>3</sup> , **Alberto Naveira Garabato**<sup>1</sup> , **Fiz F. Pérez**<sup>4</sup> , **Carl Spingys**<sup>5</sup> , **Kurt Polzin**<sup>6</sup> , and **Antón Velo**<sup>4</sup> 

<sup>1</sup>Ocean and Earth Science, National Oceanography Centre, University of Southampton, Southampton, UK, <sup>2</sup>Centro de Investigacións Mariñas, Universidade de Vigo (CIM-UVigo), Vigo, Spain, <sup>3</sup>Laboratoire d'Océanographie Physique et Spatiale (LOPS), University of Brest, CNRS, Ifremer, IRD, IUEM, Plouzané, France, <sup>4</sup>Instituto de Investigacións Mariñas, IIM-CSIC, Vigo, Spain, <sup>5</sup>National Oceanography Centre, Southampton, UK, <sup>6</sup>Woods Hole Oceanographic Institution, Woods Hole, MA, USA

**Abstract** The Atlantic Meridional Overturning Circulation entails vigorous thermohaline transformations in the subpolar North Atlantic Ocean (SPNA). There, warm and saline waters originating in the (sub)tropics are converted into cooler and fresher waters by a combination of surface fluxes and sub-surface mixing. Using microstructure measurements and a small-scale variance conservation framework, we quantify the diapycnal and isopycnal contributions –by microscale turbulence and mesoscale eddies, respectively– to thermohaline mixing within the eastern SPNA. Isopycnal stirring is found to account for the majority of thermal (65%) and haline (84%) variance dissipation in the upper 400 m of the eastern SPNA. A simple dimensional analysis suggests that isopycnal stirring could account for  $\mathcal{O}(5\text{--}10)$  Sv of diahaline volume flux, suggesting an important role of such stirring in regional water-mass transformations. Our mixing measurements are thus consistent with recent indirect estimates in highlighting the importance of isopycnal stirring for North Atlantic overturning.

**Plain Language Summary** The North Atlantic hosts an ocean circulation system called the Atlantic Meridional Overturning Circulation (AMOC). It is often likened to a giant conveyor belt in the ocean, moving warm, salty waters from south to north and transforming them into cold, fresh waters that flow back southward at greater depth. The AMOC is a crucial element of the Earth's climate, and if it were to slow down, it could lead to major climatic changes. For a long time, scientists thought that the AMOC was mainly driven by cooling in the North Atlantic. But recently, we have discovered that the mixing of different water masses is also important. In our study, we used small-scale measurements of ocean properties to examine the processes behind this mixing. Our findings show that large swirling flows known as mesoscale eddies, which are tens to hundreds of kilometers wide and hundreds of meters deep, play a dominant role in mixing heat and salt in the North Atlantic. This discovery helps us to better understand the AMOC and its future behavior.

## 1. Introduction

The subpolar North Atlantic (SPNA) is a hotspot of ocean ventilation, resulting in significant exchanges of heat and greenhouse gases with the atmosphere (Pérez et al., 2013). This makes the SPNA an important region in the regulation of Earth's climate. The relevance of the SPNA for ocean ventilation and climate is rooted in its central role in the global meridional overturning circulation (MOC) (Danialt et al., 2016; Lozier et al., 2019). Within the cyclonic pathways of the SPNA gyre, vigorous water mass transformations convert warm and salty central waters into cooler, fresher and denser subpolar mode waters (SPMW) (Brambilla & Talley, 2008; Berglund et al., 2023; García-Ibáñez et al., 2015; McCartney & Talley, 1982) and intermediate waters. These intermediate waters are formed through deep convection in the Irminger (De Jong et al., 2012; Pickart et al., 2003) and Labrador Seas (Lazier et al., 2002). Together with denser overflows from the Nordic Seas, SPNA-produced waters constitute the lower limb of the Atlantic MOC (AMOC), which flows southward within a Deep Western Boundary Current along the North American margin (Danialt et al., 2016; Lozier et al., 2019).

Traditionally, deep convection in the Labrador Sea was considered the primary source of dense water for the AMOC. However, recent observations and modeling studies have led to a paradigm shift, by which the majority

© 2024. The Author(s).

This is an open access article under the terms of the [Creative Commons Attribution License](https://creativecommons.org/licenses/by/4.0/), which permits use, distribution and reproduction in any medium, provided the original work is properly cited.

**Writing – original draft:**

Bieito Fernández Castro

**Writing – review & editing:**

Bieito Fernández Castro, Daniel Fernández Román, Bruno Ferron, Marcos Fontela, Pascale Lherminier, Alberto Naveira Garabato, Fiz F. Pérez, Carl Spingys, Kurt Polzin, Antón Velo

of the light-to-dense water mass conversion driving the AMOC is recognized to occur in the eastern SPNA (eSPNA), specifically in the Irminger and Nordic Seas (Lozier et al., 2019; Petit et al., 2020; Yeager et al., 2021). Further, while conventional understanding portrays the AMOC as an intrinsically diapycnal process, recent investigations suggest that water-mass transformations in the SPNA involve large density-compensated (isopycnal) temperature and salinity changes (Evans et al., 2023; Zou et al., 2020).

Finally, closure of the AMOC in the SPNA has been traditionally attributed to atmospheric cooling (Marsh, 2000; Petit et al., 2020), yet there is growing evidence that interior thermohaline transformations, driven by mixing along and across density surfaces, are necessary for sustaining the AMOC (Bebieva & Lozier, 2023; Brüggemann & Katsman, 2019; Berglund et al., 2023; Evans et al., 2023; Mackay et al., 2020; Tooth et al., 2023; Xu et al., 2018). Diapycnal mixing contributes, for example, to the densification of SPMW through entrainment of overflow waters (Evans et al., 2023). In turn, mixing associated with isopycnal eddy stirring delivers salt into the subpolar gyre, enabling an increase in the density of lower-limb waters (Born et al., 2016; Evans et al., 2023; Pradal & Gnanadesikan, 2014; Warren, 1983). Finally, mesoscale eddies transfer, via advection and mixing, intermediate waters produced by deep convection in the Labrador and Irminger basins into the Deep Western Boundary Current, thereby connecting such waters to the AMOC (Brüggemann & Katsman, 2019; Mackay et al., 2020; Straneo, 2006).

Despite the increasingly acknowledged importance of interior thermohaline transformations in the SPNA, direct observations in the area are scarce (Ferron et al., 2014; Jurado, Dijkstra, & van der Woerd, 2012; Jurado, van der Woerd, & Dijkstra, 2012; Kunze et al., 2023; Lauderdale et al., 2008), and quantification relies largely on indirect mixing estimates via inverse methods and model output analyses (Evans et al., 2023; Mackay et al., 2020; Tooth et al., 2023; Xu et al., 2018). Consequently, the nature of the processes driving these transformations remains largely unknown.

Mixing—the destruction of property contrasts by molecular diffusion—results from a downscale variance cascade driven by the stirring of isopycnal property gradients by mesoscale eddies (horizontal scale >10 km), and the mixing of diapycnal property gradients by microscale turbulence (horizontal and vertical scales <10 m) (Ferrari & Polzin, 2005; Garrett, 2001; Lee et al., 1997; Naveira Garabato et al., 2016). The small- and mesoscale regimes are underpinned by different dynamics, and are likely to exhibit distinct sensitivities to changes in forcing and potential feedbacks on the AMOC. A deeper understanding of SPNA mixing processes is thus essential for unraveling the AMOC's dynamics and long-term evolution.

Pioneering work in the Southern Ocean demonstrates that microstructure turbulence observations can be used to elucidate the links between mixing, thermohaline transformations and overturning circulation, and to identify the processes responsible for such mixing (Naveira Garabato et al., 2016; Orúe-Echevarría et al., 2023). In this study, we address the role of mixing in SPNA thermohaline transformations by analyzing a set of microstructure temperature and shear profiles, collected across the eSPNA, within a tracer variance budget framework (Ferrari & Polzin, 2005; Naveira Garabato et al., 2016), allowing us to disentangle the diapycnal and isopycnal contributions to mixing. Our analysis reveals that isopycnal stirring dominates thermal and, more distinctly, haline mixing in the upper layers of the eSPNA, indicating an important contribution of mesoscale turbulence to the water-mass transformations responsible for the AMOC's closure in the SPNA.

## 2. Methods

### 2.1. Observations

Microstructure data were collected during the BOCATS2 2023 cruise across the North Atlantic Ocean from 9th June to 11th July 2023. The mission sampled the OVIDE (Observatoire de la Variabilité Interannuelle à DÉcennale) repeated hydrography section (WOCE A25) between Portugal and Cape Farewell (Greenland) (Lherminier et al., 2010, 2023), and two additional sections across the East Greenland Current (EGC) and the Irminger Sea, north of the A25-OVIDE line (Figure 1a). Microstructure turbulence profiles were collected in 32 stations with a microstructure profiler (MSS, Prandke and Stips (1998)). A total of 94 profiles were obtained, with 1–3 profiles per station, except in the last station (station 32) over the Reykjanes Ridge at 61.14°N, 27.97°W.

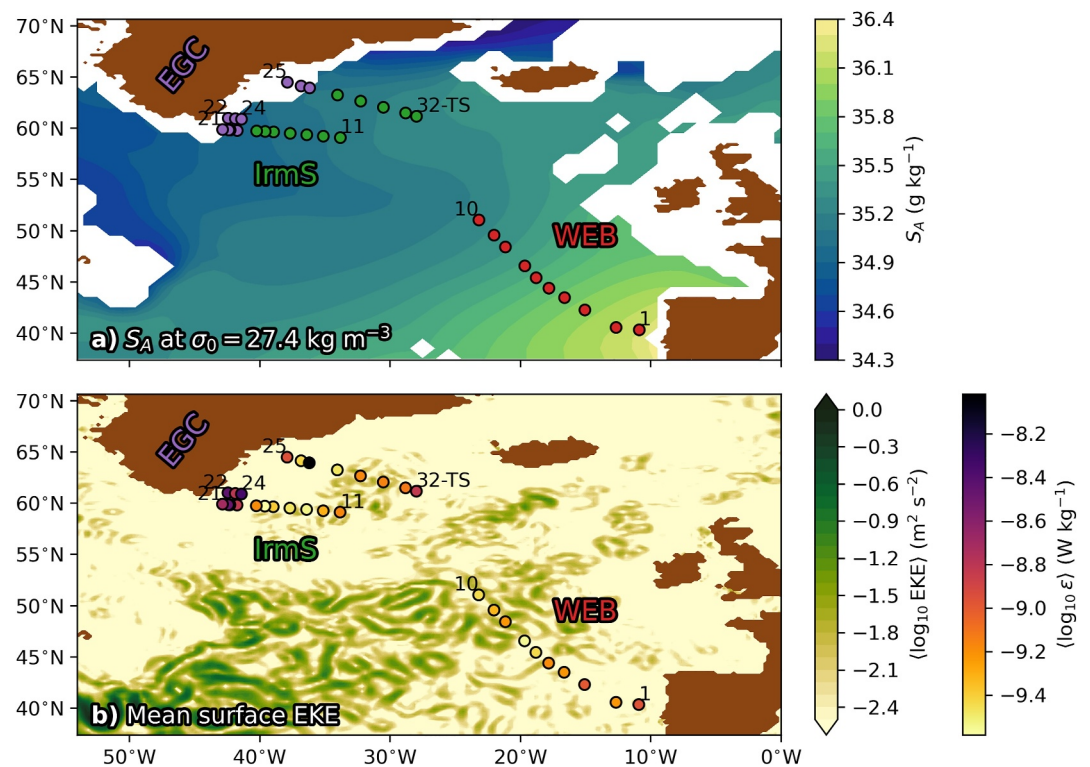


**Figure 1.** Maps of the BOCATS2 cruise microstructure stations. Dots indicate the station positions and are color-coded by (a) sampling region (Red: Western European Basin, WEB, stations 1–10; Green: Irminger Sea, IrmS, stations 11–17, 28–32; Purple: East Greenland Current, EGC, stations 18–27), and (b) mean value of  $\epsilon$  below 50 m depth. Station numbers for the beginning and end of each sub-transect are shown, together with labels for the three analysis regions. The background contours represent: (a) climatological absolute salinity  $S_A$  distribution at the  $\sigma_0 = 27.4 \text{ kg m}^{-3}$  isopycnal based on the World Ocean Atlas 2018 (Boyer et al., 2018), (b) mean satellite-derived eddy kinetic energy over the cruise duration (data set dataset-duacs-nrt-global-merged-allsat-phy-14 from <https://marine.copernicus.eu>). The basin-scale contrast of salinity on an isopycnal (a) illustrates the large density-compensated thermohaline gradients characterizing in this region, which provide necessary conditions for isopycnal stirring to have a relevant contribution to mixing.

There, a time-series consisting of 21 profiles was recorded during a 14-hr period (TS label in Figure 1). Profiles were performed down to depths of 300–400 m, except in shallower stations of the EGC.

The MSS is equipped with two shear microstructure sensors and a temperature microstructure sensor, complemented with a Sea&Sun high-accuracy Conductivity-Temperature-Depth (CTD) suite. The instrument is loosely tethered and operates in free-falling mode at a vertical speed of  $0.6\text{--}0.7 \text{ m s}^{-1}$ , sampling all variables at 1,024 Hz. Profiles of conservative temperature ( $\Theta$ ), practical salinity ( $S_A$ ) and surface-referenced potential density ( $\sigma_\theta$ ) with 1 m vertical resolution were derived by bin-averaging the CTD output. The dissipation rates of turbulent kinetic energy ( $\epsilon$ ) and thermal variance ( $\chi_\Theta$ ) were computed from the microstructure shear and temperature measurements, respectively, with a vertical resolution of 1 m from overlapping data segments of 4 m length following Piccolroaz et al. (2021) and Fernández Castro et al. (2022).

Generally,  $\epsilon$  and  $\chi_\Theta$  were determined by integration of the shear and temperature gradient spectra over the well-resolved wavenumber ranges, and the variance outside those ranges was recovered using empirical spectral forms (Nasmyth and Kraichnan, respectively) (Fernández Castro et al., 2022). Pairs of measured shear and temperature spectra, randomly selected over the range of representative values, are presented in Figure 2, showing a good agreement with the corresponding empirical spectra. Due to weak turbulence, shear-based  $\epsilon$  estimates occasionally approached the instrument's noise floor of  $\mathcal{O}(10^{-9} \text{ W kg}^{-1})$ . In those instances,  $\epsilon$  was derived through fitting the temperature gradient spectrum to the Kraichnan spectrum (Piccolroaz et al., 2021), as this technique has a lower noise floor of  $\mathcal{O}(10^{-12} \text{ W kg}^{-1})$ . For consistency, in those instances  $\chi_\Theta$  was also derived from spectral fits.

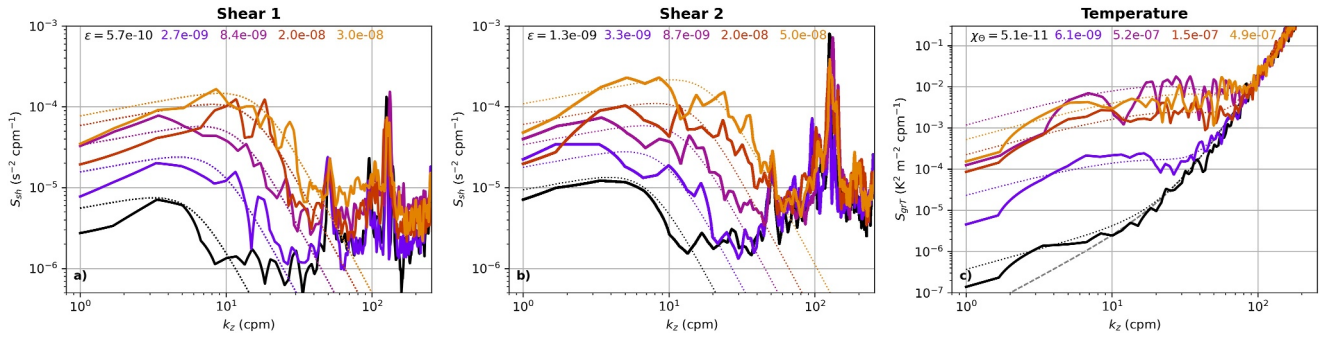
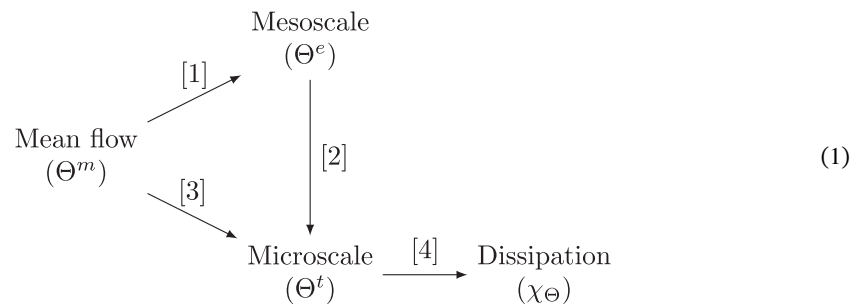


**Figure 2.** Microstructure spectra. Randomly selected vertical wavenumber ( $k_z$ ) spectra, from shear sensor 1 (a), shear sensor 2 (b), and thermistor (c), respectively, and for  $\epsilon$  values in the range  $10^{-10} - 10^{-6} \text{ W kg}^{-1}$ . Dotted lines show the corresponding empirical spectra obtained through spectral integration (shear) or fitting to the Kraichnan spectrum (temperature). The thermistor's theoretical noise curve is shown as a gray dashed line. The derived  $\epsilon$  ( $\text{W kg}^{-1}$ ) and  $\chi_\theta$  ( $\text{K}^2 \text{ s}^{-1}$ ) values are reported.

### 2.2. Triple Decomposition of the Tracer Variance Budget: Theory

To investigate the relative contribution of small- and mesoscale turbulence to thermohaline mixing, we followed a triple decomposition of the small-scale tracer variance conservation equation (Davis, 1994; Ferrari & Polzin, 2005; Garrett, 2001; Joyce, 1977). This decomposition is founded on the interpretation of mixing as a tracer variance transfer from the basin scale (where variance is introduced, e.g., by air-sea fluxes) to centimeter scales, where it is dissipated by molecular processes. The variance cascade follows two main pathways, mediated by mesoscale and microscale turbulence, respectively, as summarized in a diagram proposed by Garrett (2001):



Here, we used conservative temperature ( $\Theta$ ) as our reference tracer, and decomposed the spatio-temporal distribution of  $\Theta$  into the sum of three terms,  $\Theta = \Theta^m + \Theta^e + \Theta^t$ .  $\Theta^m$  represents the large-scale, slowly varying (typically  $>100 \text{ km}$  in the horizontal,  $>100 \text{ m}$  in the vertical, months to years and over, in time) mean distribution of temperature;  $\Theta^e$  represents mesoscale ( $10\text{--}100 \text{ km}$  in the horizontal,  $10\text{--}100 \text{ m}$  in the vertical, days to months in time) fluctuations;  $\Theta^t$  are the microscale ( $<10 \text{ m}$  in space, seconds to hours in time) fluctuations associated with isotropic turbulence; and  $\chi_\theta$  is the rate of thermal variance dissipation by molecular processes.

In the microscale pathway ([3]  $\rightarrow$  [4]), microscale isotropic turbulence transfers tracer variance from the mean flow directly into microscale variability ( $\Theta^t$ ) and dissipation. This transfer is mediated by microscale overturns of the mean vertical density profile, that is, through stirring of the diapycnal tracer gradient. The mesoscale route ([1]  $\rightarrow$  [2]  $\rightarrow$  [4]) starts with the stirring of tracer gradients along isopycnal surfaces, which results in the creation of vertical fine-scale structures in the range of  $10\text{--}100 \text{ m}$  (Figure 3). The variance stored in such mesoscale fluctuations ( $\Theta^e$ ) is finally transferred to dissipation scales by microscale overturning turbulence.

Traditionally, microstructure studies have focused on the variance transfer to the microscale and dissipation (the combined effect of [2] + [3], leading to [4]) and expressed the tracer variance conservation equation in a two-term Reynolds decomposition framework. In this framework, the flow components are separated into the sum of turbulent fluctuations ( $<10 \text{ m}$ ) and a mean flow component ( $\Theta = \bar{\Theta} + \Theta^t$ ), which includes both the large-scale

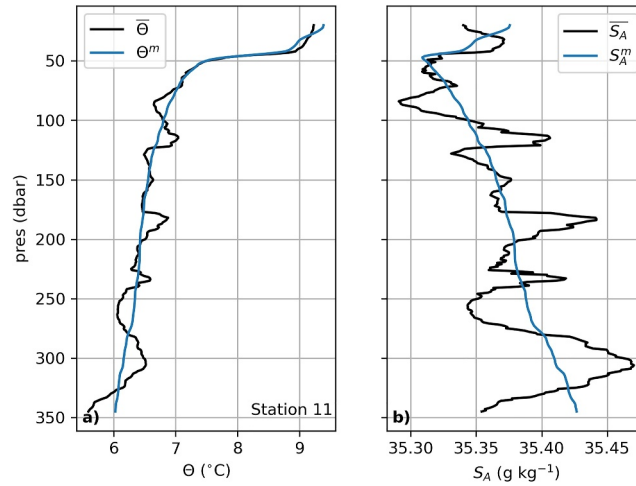


**Figure 3.** Obtaining the background profiles. Example profile (station 11, profile 2), showing results from the polynomial fit (Equation 7) used to obtain the background (or large-scale mean flow, in the conventional terminology) profiles of conservative temperature ( $\Theta^m$ , a) and absolute salinity ( $S_A$ , b) from the CTD-observed profiles ( $\bar{\Theta}$  and  $\bar{S}_A$ , respectively). These profiles exhibit pronounced density-compensated thermohaline fine-scale structures resulting from eddy stirring. Such structures are effectively removed by the polynomial fit of the corresponding tracer against potential density.

mean flow and mesoscale fluctuations ( $\bar{\Theta} = \Theta^m + \Theta^e$ ). In practice, in oceanographic studies, turbulent fluctuations ( $\Theta^e$ ) are defined as those related to microscale three-dimensional turbulence ( $<10$  m), which results in diapycnal tracer mixing, and can only be measured with microstructure instruments. The mean flow component ( $\bar{\Theta}$ ) covers multi-meter scales of variability, which are resolved by standard (CTD) oceanographic measurements. The latter  $\bar{\Theta}$  includes the basin-scale tracer contrasts, but also fine-scale structures due to stirring by mesoscale motions along isopycnal surfaces (Ferrari & Polzin, 2005).

In the two-term Reynolds framework, and in the limit of flow and tracer fluctuations being statistically stationary and homogeneous, the tracer variance conservation is expressed as:

$$\underbrace{-2\mathbf{u}'\Theta'}_{P_{\Theta^2}} \cdot \nabla \bar{\Theta} = 2\kappa_{\Theta} \underbrace{(\nabla \bar{\Theta})^2}_{\chi_{\Theta}} \quad (2)$$

where  $\mathbf{u}$  is the flow velocity,  $\nabla$  is a three-dimensional gradient operator, and  $\kappa_{\Theta}$  is the molecular diffusivity of heat. This equation expresses a local balance between the production of small-scale tracer variance,  $P_{\Theta^2}$ , due to the stirring of the mean-flow three-dimensional tracer gradient ( $\nabla \bar{\Theta}$ ) by turbulent eddies (which results from the combined downscale transfer via the mesoscale and microscale routes, [1] + [3]), and its dissipation by molecular diffusion,  $\chi_{\Theta}$  or [4].

By taking a gradient flux approximation ( $\mathbf{u}'\Theta' = -K_{\rho}\nabla\bar{\Theta}$ ), and using the facts that diapycnal gradients are much larger than isopycnal gradients and isopycnal layers are close to horizontal ( $|\nabla\bar{\Theta}| \approx |\partial\bar{\Theta}/\partial z|$ ), tracer variance dissipation can be related to a microscale turbulent diapycnal diffusivity ( $K_{\rho}$ ) via the widely used Osborn and Cox (1972) formula:

$$\chi_{\Theta} = P_{\Theta^2} \approx 2K_{\rho} \left( \frac{\partial \bar{\Theta}}{\partial z} \right)^2 \quad (3)$$

The triple variance decomposition allows one to separately account for the contributions of mesoscale (isopycnal) stirring and microscale turbulence (diapycnal mixing) to the variance cascade. In this framework, the tracer variance conservation equation is expressed as (Ferrari & Polzin, 2005):

$$-2\underbrace{\langle \mathbf{u}'\Theta' \rangle \cdot \nabla_{\perp} \Theta^m}_{P_{\Theta^2}^{\perp}} - 2\underbrace{\langle \mathbf{u}^e \Theta^e \rangle \cdot \nabla_{\parallel} \Theta^m}_{P_{\Theta^2}^{\parallel}} = \chi_{\Theta}, \quad (4)$$

where angled brackets represent an average over large spatial scales in comparison with mesoscale fluctuations, but small in comparison with the large-scale mean flow; and  $\nabla_{\perp}$  and  $\nabla_{\parallel}$  respectively denote gradient operators across and along density surfaces. In this framework, the dissipation of thermal variance [4] is thus balanced by the stirring of the mean diapycnal gradient by microscale turbulence ( $P_{\Theta^2}^{\perp}$  or [3]) plus the stirring of the large-scale isopycnal gradients by mesoscale motions ( $P_{\Theta^2}^{\parallel}$ , [1]). Mesoscale stirring generates vertical fine-scale (10–100 m) structures, whose variance is then transferred to the microscale by microscale turbulence ([2]), eventually resulting in molecular dissipation ([4]).

By applying a flux-gradient relationship,  $P_{\Theta^2}^{\perp}$  can be linked to the microscale diapycnal diffusivity:

$$P_{\Theta^2}^{\perp} = 2K_{\rho}(\nabla_{\perp} \Theta^m)^2, \quad (5)$$

and the contribution of eddy stirring to mixing can be diagnosed as:

$$P_{\Theta^2}^{\parallel} = \chi_{\Theta} - P_{\Theta^2}^{\perp} = \chi_{\Theta} - 2K_{\rho}(\nabla_{\perp} \Theta^m)^2. \quad (6)$$

### 2.3. Triple Decomposition of the Tracer Variance Budget: Implementation

By applying the variance budget framework (Equations 4–6) to BOCATS2 microstructure data, we assessed the relative contribution of microscale turbulence and mesoscale stirring to the mixing of heat (and salt) in the eSPNA. To do so, we used microstructure observations of  $\chi_{\Theta}$  to quantify total heat mixing, and we estimated the contribution of microscale turbulence by quantifying  $P_{\Theta^2}^{\perp}$  using Equation 5. We finally inferred the contribution of isopycnal stirring from the difference between  $\chi_{\Theta}$  and  $P_{\Theta^2}^{\perp}$  (Equation 6).

Quantifying the contribution of microscale turbulence to mixing (i.e., diapycnal mixing) from observed  $\bar{\Theta}$  profiles (here the overbar denotes tracer profiles measured by our profiler's CTD probe with meter-scale resolution) involves some degree of spatial or temporal averaging to remove fluctuations associated with mesoscale stirring, to estimate  $\Theta^m$  and compute  $P_{\Theta^2}^{\perp}$  via Equation 5 (Ferrari & Polzin, 2005). Such averaging is impractical in most stations of our data set, where spatio-temporal information is lacking. To overcome this limitation, we smoothed the measured profiles through a 4-degree polynomial fit against  $\sigma_0$  over the full range of measured depths, in order to obtain a set of  $\Theta^m$  profiles (see example in Figure 3):

$$\Theta^m = f(a_0 + a_1 \cdot \sigma_0 + \dots + a_4 \cdot \sigma_0^4) \quad (7)$$

Although the choice of a 4-degree polynomial is somewhat arbitrary, our results proved relatively insensitive to the precise choice or smoothing method.

This approach removes the density-compensated vertical fine-scale structures (10 – 100 m length scales) associated with isopycnal stirring. Those structures are the element connecting the mesoscale variance cascade to microscale turbulence and dissipation. Therefore, removing the vertical fine-scale structures allows one to isolate the contribution of mesoscale stirring from the observed mixing. Herewith, we refer to this particular form of  $\Theta^m$  profiles as “background” profiles, instead of the more general “large-scale mean” profiles, to avoid the ambiguity of scale in the definition of a “large-scale mean.”

The diapycnal production term (Equation 5) was then estimated using the vertical gradients of  $\Theta^m$ , assuming that isopycnals are nearly horizontal:

$$P_{\Theta^2}^{\perp} = 2K_{\rho} \left( \frac{\partial \Theta^m}{\partial z} \right)^2. \quad (8)$$

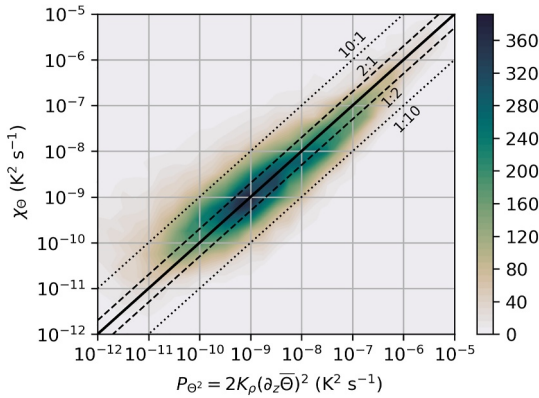


**Figure 4.** Small-scale variance production and dissipation. Two-dimensional histogram of thermal variance dissipation rate ( $\chi_{\Theta}$ ) and small-scale thermal variance production due to the action of microscale turbulent motions on the fine-scale resolved conservative temperature profile ( $P_{\Theta^2}$ ), which includes the contributions from the mean flow and the mesoscale eddy components, in the context of the triple decomposition framework. The solid line indicates a one-to-one correspondence, and the dashed and dotted lines delimit agreement within a factor of 2 and 10, respectively.

where  $\partial\bar{S}_A/\partial z$  is determined by linear fitting over 4 m segments (similar to  $\bar{N}^2$ ). This approximation assumes that  $\chi_S$  is balanced locally by the effect of stirring by microscale turbulence on fine-scale tracer gradients ( $P_S^{\perp}$ ). The assumption is clearly met for  $\Theta$ , for which  $\chi_{\Theta}$  and  $P_{\Theta^2}$  agree within a factor of 2 over 5 orders of magnitude (Figure 4), suggesting that Equation 10 is an adequate approximation for estimating  $\chi_S$ .

### 3. Results

#### 3.1. Hydrography

The BOCATS2 microstructure survey stations covered the broad range of hydrographic conditions characterizing the eSPNA, which reflect the transformation of central waters into SPMW (Brambilla & Talley, 2008; García-Ibáñez et al., 2015; McCartney & Talley, 1982; Stendardo et al., 2024). The eastern section (stations 1–10, Figure 1) sampled the relatively warm (10–20°C), salty (>35.75 g kg<sup>-1</sup>) and light ( $\sigma_0 < 27.4$  kg m<sup>-3</sup>) central waters of the Western European Basin (WEB) (Figure 5). The upper ocean (<400 m) of the WEB was strongly stratified, with a  $\sim 1$  kg m<sup>-3</sup> contrast between the upper and deeper sampled layers (Figures 5c and 6a). WEB stratification was dominated by temperature differences, whilst haline stratification was weakly unstable (Figures 5a, 5b and 6a). The western sections sampled across the Irminger Sea (IrmS) and the EGC (Figure 1). Below a shallow seasonal thermocline, IrmS waters were cooler (3–11°C) and fresher (35.0–35.6 g kg<sup>-1</sup>) than WEB waters, and also denser, with  $\sigma_0 > 27.5$  kg m<sup>-3</sup> (Figure 5), as is characteristic of SPMW (Brambilla & Talley, 2008; Stendardo et al., 2024). The upper IrmS was also thermally stratified, but more weakly than the WEB, with a density difference of  $\sim 0.7$  kg m<sup>-3</sup> (Figure 6a). The salinity profiles were rather homogeneous (Figure 5b), resulting in very weak haline stratification (Figure 6a). Finally, the offshore waters of the EGC showed a large overlap in thermohaline properties with IrmS waters, at least below 100 m depth. However, shallower depths were markedly cooler, fresher and lighter, particularly in the inner EGC, with temperatures and salinities as low as -1°C and 30 g kg<sup>-1</sup> (Figure 5). Contrary to the WEB and IrmS, the strong stratification of EGC waters (>1 kg m<sup>-3</sup> in inshore stations) was salinity-driven (Figure 6a).

Overall, BOCATS2 sampled across a northwestward gradient of decreasing temperature and salinity, which is partially density-compensated. This partial compensation permits the existence of substantial thermohaline gradients along isopycnals (as seen in the climatological  $S_A$  distribution shown in Figure 1a). Mesoscale eddies acting on these large-scale thermohaline gradients produce measurable density-compensated thermohaline vertical fine-scale structures (Figures 5a and 5b). Such fine structures make different contributions to the overall

Here, the diapycnal diffusivity was calculated using the Osborn (1980) formula:

$$K_{\rho} = \Gamma \frac{\epsilon}{\bar{N}^2} \quad (9)$$

where  $\Gamma$  is the mixing efficiency, assumed to take a constant value of  $\Gamma = 0.2$  (Oakey, 1982), and  $\bar{N}^2 = -g/\rho\partial\bar{\rho}/\partial z$  is the buoyancy frequency. The density gradient is calculated by linear fitting of the measured density profile against depth over 4 m segments (the same vertical scale over which  $\epsilon$  and  $\chi_{\Theta}$  are calculated).

The same diagnosis of the mixing contributions was performed for salinity. However, while  $P_S^{\perp}$  is computed in the same way as  $P_{\Theta^2}$ ,  $\chi_S$  could not be obtained directly from microstructure salinity observations as those were not available. We circumvented this issue by using the Osborn and Cox (1972) formula (Equation 3) to estimate  $\chi_S$  from  $K_{\rho}$  and the fine-scale vertical salinity gradient as measured by the microprofiler's CTD suite ( $\partial\bar{S}_A/\partial z$ ):

$$\chi_S \approx 2K_{\rho} \left( \frac{\partial\bar{S}_A}{\partial z} \right)^2, \quad (10)$$

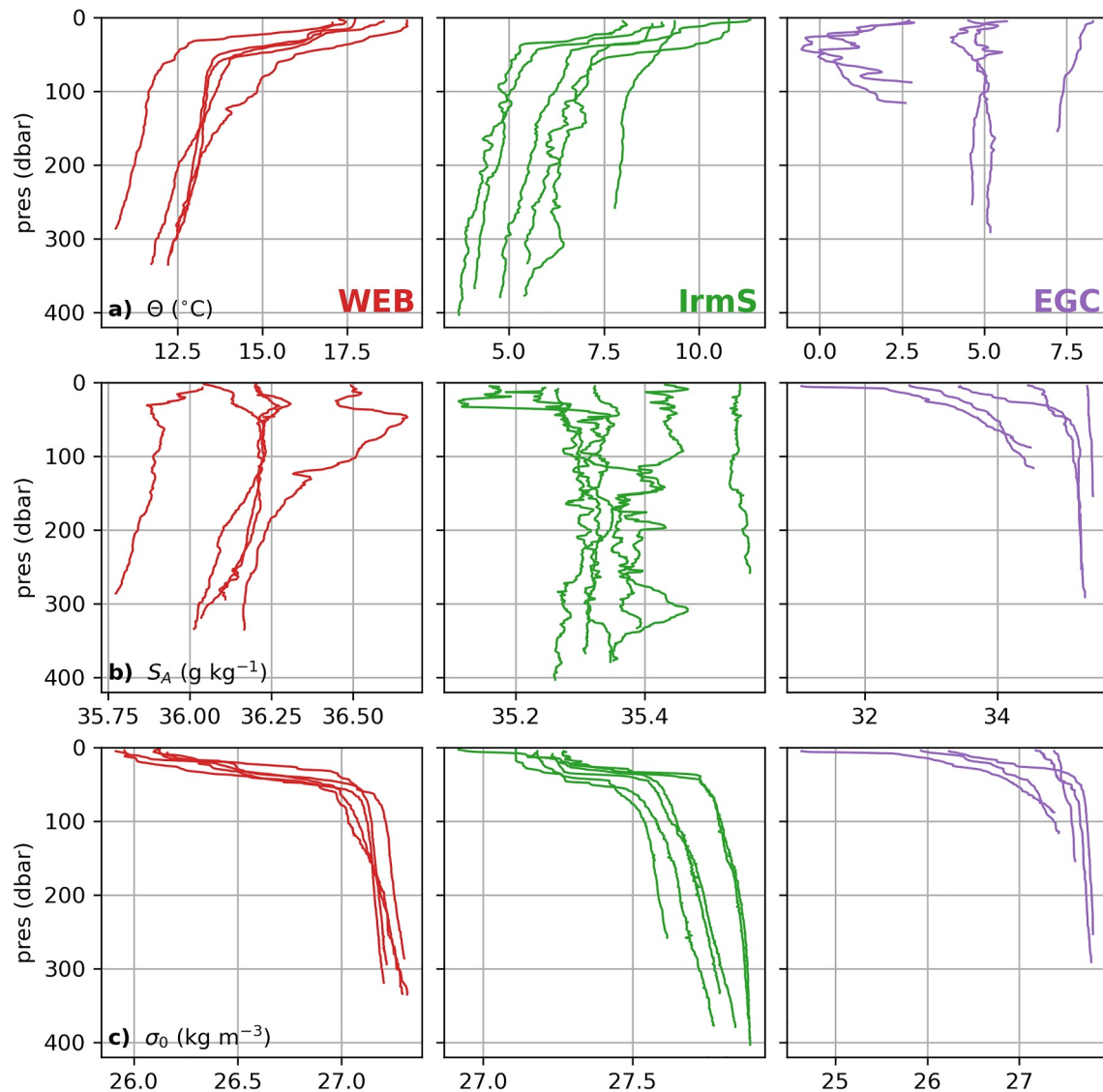


**Figure 5.** Hydrographic profiles. Example profiles of (a) conservative temperature ( $\Theta$ ), (b) absolute salinity ( $S_A$ ) and (c) potential density ( $\sigma_0$ ) during the BOCATS2 cruise. One profile is shown for every other sampled station. Profiles are color coded by region (Red: Western European Basin, WEB; Green: Irminger Sea, IrmS; Purple: East Greenland Current, EGC).

vertical variance of  $\Theta$  and  $S_A$  in different regions (Figure 6b), reflecting the relative importance of isopycnal stirring. Due to the strong thermal stratification in the WEB and IrmS, almost 100% of the  $\Theta$  vertical variance corresponds to the background profile ( $\Theta^m$ ), although density-compensated fine-scale thermal structures associated with eddy stirring were also evident there (Figure 5a). Fine-scale structures had a larger imprint on salinity vertical variance in those same regions, where the background salinity profile ( $S_A^m$ ) contained only 50%–80% of the  $S_A$  variance, due to the weak salinity stratification (Figure 6b). The reverse scenario was encountered in the salinity-stratified EGC region, where most of  $S_A$  variance was explained by  $S_A^m$ , and  $\Theta$  fine structures made a variable but larger (up to 50%) contribution to thermal variance.

### 3.2. Isopycnal Stirring and Diapycnal Mixing From a Time-Series Station

The occurrence of density-compensated thermohaline fine structures, and their temporal variability, is clearly illustrated in the 14-hr time-series station data at the Reykjanes Ridge (Figure 7). As the rest of the IrmS, the sampling site was thermally stratified with a thermocline at around 50 m depth (Figure 7a), while salinity did not



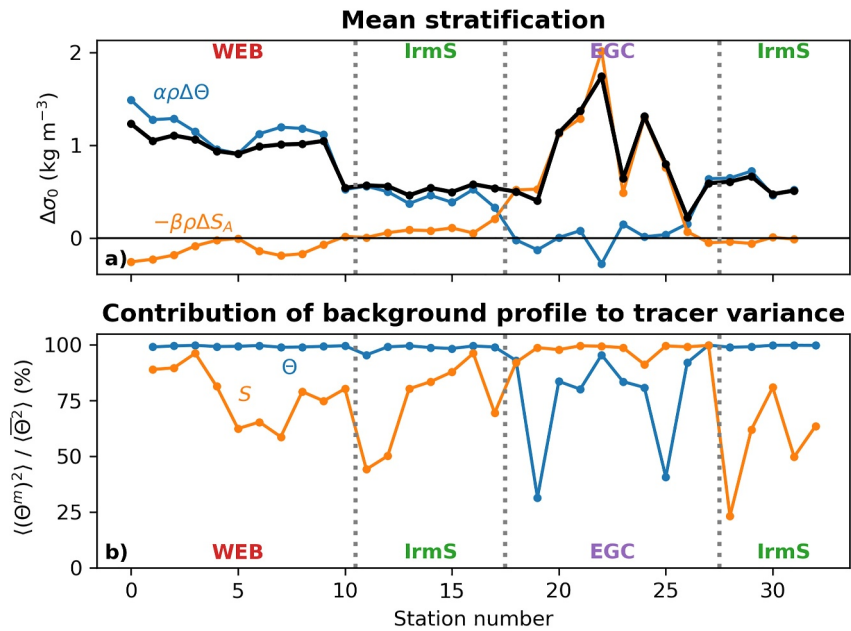


**Figure 6.** Stratification and vertical tracer variance. (a) Density difference between the top and the bottom of the MSS profile at each station ( $\Delta\sigma_0$ , black), alongside partial contributions from temperature ( $\alpha\rho\Delta\Theta$ ) and salinity ( $-\beta\rho\Delta S_A$ ). (b) Ratio between the variance of the background (or “large-scale mean”) component of  $\Theta$  (blue) (and  $S_A$ , orange),  $\langle(\Theta^m)^2\rangle$ , to the total variance of the measured  $\Theta$  (and  $S_A$ ) profiles,  $\langle(\Theta)^2\rangle$ .

exhibit a well-defined mean vertical structure (Figure 7b). Instead, there was substantial temporal and vertical fine-scale variability (Figures 7b and 7d). Although some isopycnal heaving was apparent, thermohaline variability occurred mostly at constant density, as salinity anomalies were mirrored by opposing temperature anomalies (Figures 7c and 7d). The site was rather turbulent, with  $\epsilon$  and  $\chi_\Theta$  values of  $10^{-8} - 10^{-7} \text{ W kg}^{-1}$  and  $10^{-7} - 10^{-6} \text{ K}^2 \text{ s}^{-1}$  in the surface layer and thermocline, and recurrent patches of comparably intense turbulence and mixing in deeper layers (Figures 7a and 7b).

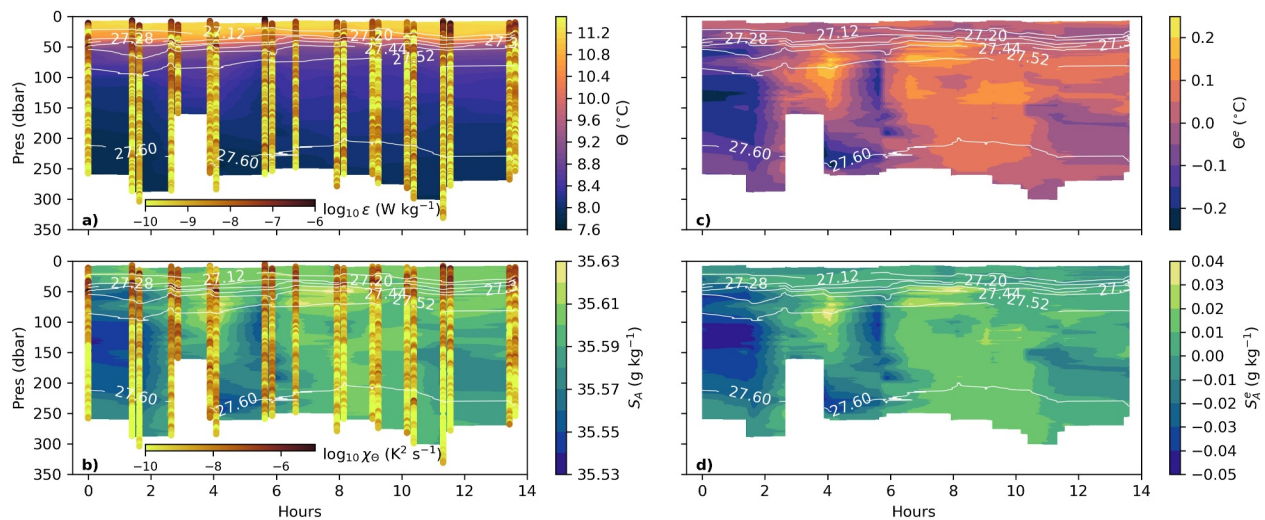


**Figure 7.** Hydrographic profiles at time-series station 32 over the Reykjanes Ridge. (a, b) 14-hr time-series of conservative temperature ( $\Theta$ ) and practical salinity ( $S_A$ ) vertical profiles, with potential density contours (white) overlaid. Profiles of the dissipation rates of turbulent kinetic energy ( $\epsilon$ ) and thermal variance ( $\chi_\Theta$ ) are shown as colored dots in (a) and (b), respectively. (c, d) Conservative temperature and salinity mesoscale anomaly profiles ( $\Theta^e$ ,  $S_A^e$ , respectively), computed with respect to the time-mean profiles in  $\sigma_0$  coordinates.

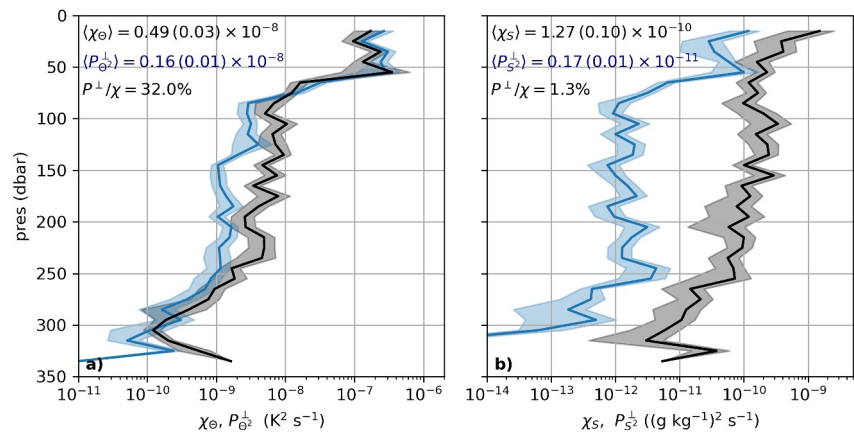


**Figure 8.** Mixing rates at time-series station 32 over the Reykjanes Ridge. Time-mean profiles of the dissipation rates of thermal (a) and salinity (b) variance ( $\chi_{\theta}$ ,  $\chi_s$ , black), along with small-scale variance production by microscale turbulence ( $P_{\theta^2}^{\perp}$ ,  $P_{s^2}^{\perp}$ , blue). Error bars (shading) represent  $\pm 2$  standard errors. Mean values of  $\chi$  and  $P^{\perp}$  below 100 m depth, and their ratio, are reported.

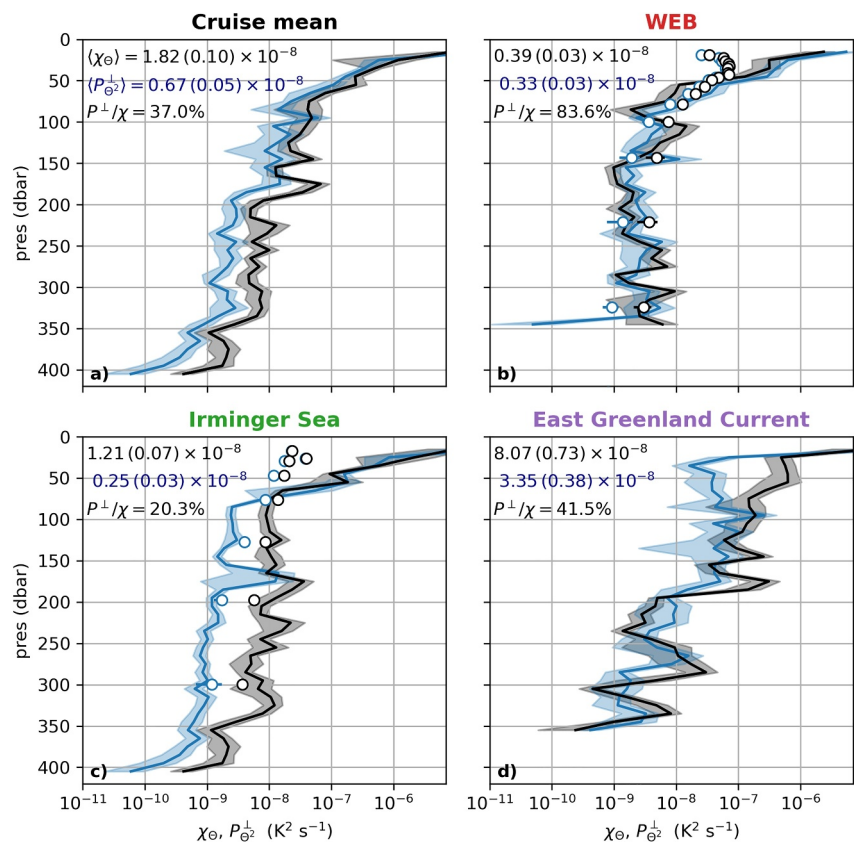


**Figure 9.** Cruise-mean thermal mixing rate profiles. Mean profiles (solid lines) of the dissipation rates of thermal variance ( $\chi_{\theta}$ ), along with small-scale variance production by microscale turbulence ( $P_{\theta^2}^{\perp}$ , blue) for the entire cruise (a), and for the different analysis regions: Western European Basin, WEB (b); Irminger Sea, IrmS (c); East Greenland Current, EGC (d). Error bars (shading) represent  $\pm 2$  standard errors. Mean values of  $\chi$  and  $P^{\perp}$  below 100 m depth, and their ratio, are reported. Dots show estimates of  $P_{\theta^2}^{\perp}$  and  $\chi_{\theta}$  (computed as  $\chi_{\theta} = P_{\theta^2}^{\perp} + P_{\theta^2}^{\parallel}$ ) from climatological temperature fields (Boyer et al., 2018) and global diffusivity databases (de Lavergne et al., 2020; Groeskamp et al., 2020).

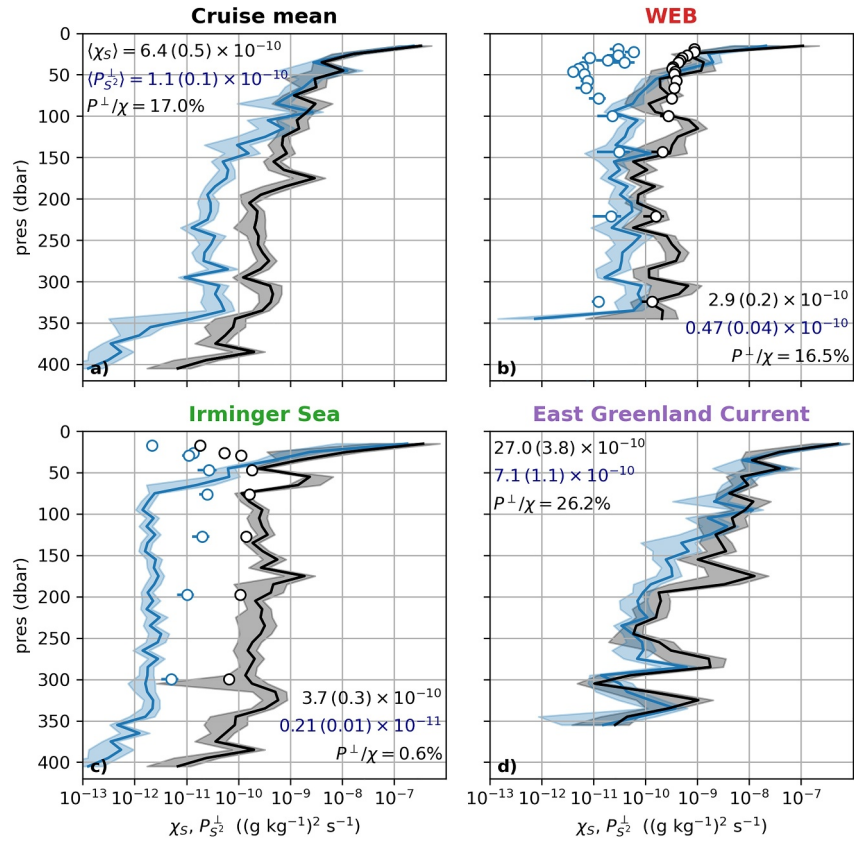


**Figure 10.** Cruise-mean haline mixing rate profiles. Mean profiles (solid lines) of the dissipation rates of salinity variance ( $\chi_s$ , black), along with small-scale variance production by microscale turbulence ( $P_{s^2}^\perp$ , blue) for the entire cruise (a, f), and for the different analysis regions: Western European Basin, WEB (b); Irminger Sea, IrmS (c); East Greenland Current, EGC (d). Error bars (shading) represent  $\pm 2$  standard errors. Mean values of  $\chi$  and  $P^\perp$  below 100 m depth, and their ratio, are reported. Dots show estimates of  $P_{s^2}^\perp$  and  $\chi_s$  (computed as  $\chi_s = P_{s^2}^\perp + P_{s^2}^\parallel$ ) from climatological salinity fields (Boyer et al., 2018) and global diffusivity databases (de Lavergne et al., 2020; Groeskamp et al., 2020).

The mean rates of thermal variance dissipation ( $\chi_\theta$ —from microstructure measurements) and diapycnal production ( $P_{\theta^2}^\perp$ , Equation 5), were similar at  $10^{-7}$  K<sup>2</sup> s<sup>-1</sup> in the shallow thermocline (Figure 8a), indicating a dominance of thermal mixing by microscale turbulence. However, below 100 m depth,  $\chi_\theta$  was consistently higher than  $P_{\theta^2}^\perp$ , due to the intensification of thermal mixing associated with fine-scale eddy-induced variability. When averaged below 100 m,  $P_{\theta^2}^\perp$  ( $0.16 \times 10^{-8}$  K<sup>2</sup> s<sup>-1</sup>) accounted for about one third of the overall  $\chi_\theta$  ( $0.49 \times 10^{-8}$  K<sup>2</sup> s<sup>-1</sup>) (Figure 8a). Therefore, eddy stirring was the main driver of thermal mixing below the seasonal thermocline. Due to the lack of a well-defined background diapycnal salinity gradient, the contribution of eddy stirring to salinity mixing was overwhelmingly dominant, even within the thermocline (Figure 8b), as diapycnal production ( $P_{s^2}^\perp = 0.17 \times 10^{-11}$  (g kg<sup>-1</sup>)<sup>2</sup> s<sup>-1</sup>) explained only 1.3% of the haline variance dissipation ( $\chi_s = 1.27 \times 10^{-10}$  (g kg<sup>-1</sup>)<sup>2</sup> s<sup>-1</sup>).

### 3.3. Regional Patterns in Isopycnal Stirring and Diapycnal Mixing

The analysis of all the microstructure profiles recorded during BOCATS2 was consistent with the overall dominance of mesoscale stirring below the seasonal pycnocline ( $\sim 100$  m), for both temperature and salinity mixing (Figures 9a and 10a). On average, microscale turbulence accounted for 37% of the observed mean  $\chi_\theta$  ( $1.82 \times 10^{-8}$  K<sup>2</sup> s<sup>-1</sup>), and for 17% of the mean  $\chi_s$  ( $6.4 \times 10^{-10}$  (g kg<sup>-1</sup>)<sup>2</sup> s<sup>-1</sup>). The cruise-mean values encapsulate substantial regional differences in both the intensity of mixing and the relative importance of diapycnal and isopycnal processes.

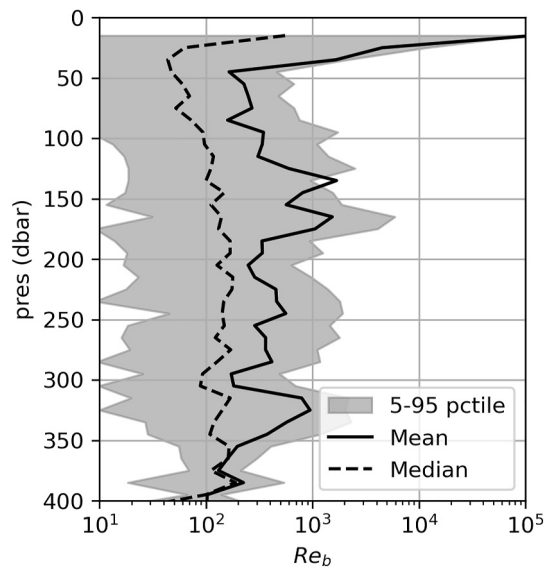


**Figure 11.** Turbulence regimes. Cruise-averaged profiles of the buoyancy Reynolds number ( $Re_b = \epsilon/(\nu N^2)$ , where  $\nu$  is molecular viscosity) estimated over 10 m bins. The arithmetic mean and median profiles are shown as solid and dashed lines, respectively, and the gray shading delimits the 5th and 95th percentiles.

At the WEB, mixing below the seasonal thermocline was weaker than the cruise mean, at  $\chi_\theta = 0.39 \times 10^{-8} \text{ K}^2 \text{ s}^{-1}$  and  $\chi_S = 2.9 \times 10^{-10} (\text{g kg}^{-1})^2 \text{ s}^{-1}$  (Figures 9b and 10b). In this thermally stratified basin, diapycnal production was sufficient to explain almost all (84%) of the observed thermal mixing (Figure 9b), while its contribution to salinity mixing was close to the cruise-average value of 17% (Figure 10b). The IrmS was characterized by intermediate variance destruction rates of  $\chi_\theta = 1.21 \times 10^{-8} \text{ K}^2 \text{ s}^{-1}$  and  $\chi_S = 3.7 \times 10^{-10} (\text{g kg}^{-1})^2 \text{ s}^{-1}$  and a dominant role of isopycnal stirring, as diapycnal production accounted for only 20% and 0.6% of the thermal and haline mixing, respectively (Figures 9c and 10c). In the EGC region, where turbulent kinetic energy dissipation rates were large (Figure 1b), the highest levels of mixing were observed at  $\chi_\theta = 8.07 \times 10^{-8} \text{ K}^2 \text{ s}^{-1}$  and  $\chi_S = 27.0 \times 10^{-10} (\text{g kg}^{-1})^2 \text{ s}^{-1}$  (Figures 9d and 10d). In this salinity-stratified area, the relative contribution of diapycnal haline mixing was the highest of the cruise at 26%. The mean contribution of diapycnal mixing to thermal variance dissipation sat at intermediate values of 42% below the halocline. However, within the halocline, thermal mixing was largely associated with isopycnal stirring, consistent with the sharp fine-scale thermal structures observed there (Figure 5a).

## 4. Limitations

### 4.1. Validity of Assumptions

The triple decomposition framework employed in this study has great potential to unravel the contributions of microscale and mesoscale turbulence to mixing; however, the method relies on several assumptions and choices entailing uncertainties and potential biases. Here, we assess to which extent our main conclusions may be impacted by such uncertainties.

One key assumption is that the mixing efficiency is relatively constant at  $\Gamma = 0.2$ , which enables estimation of the diapycnal variance production ( $P_{\theta^2}^\perp$ ) via Equations 8 and 9. The validity of this assumption is strongly supported by the good agreement, throughout the cruise data set, between thermal variance dissipation ( $\chi_\theta$ ) and its production via turbulent stirring of fine-scale gradients ( $P_{\theta^2}$ ) (Figure 4), since the estimation of  $P_{\theta^2}$  involves the use of a constant  $\Gamma = 0.2$  in Equation 9. The relative constancy of the mixing efficiency is consistent with the dominant regime of turbulence in the region. An evaluation of the buoyancy Reynolds number ( $Re_b = \epsilon/(\nu N^2)$ , where  $\nu \approx 10^{-6} \text{ m}^2 \text{ s}^{-1}$  is molecular viscosity) shows that the vast majority of  $Re_b$  values were in the range 10–1,000 (Figure 11), indicative of intermediate to energetic turbulence conditions. In such range, mixing efficiency is expected to be almost constant at  $\sim 0.2$  (Ijichi et al., 2020).

The estimation of  $\chi_S$  via the Osborn and Cox (1972) formula (Equation 10), by equating it to  $P_{S^2}$ , involves the additional assumption that variance dissipation ( $\chi_S$ ) is balanced locally by production via turbulent stirring of fine-scale (1–10 m) gradients ( $P_{S^2}$ ), in the context of the two-term Reynolds decomposition. Therefore, the temporal variability and advection terms in the small-scale variance conservation equation are neglected. A local balance between variance dissipation and production by microscale turbulence is also required for the computation of the diapycnal mixing rates ( $P^\perp$ ) via Equation 8 and, therefore, for our estimation of the relative contributions of microscale and mesoscale processes to mixing. The validity of this assumption is again strongly endorsed by the good agreement between  $\chi_\theta$  and  $P_{\theta^2}$  (Figure 4). To further ascertain the robustness the local production-dissipation balance and the approximation of  $\chi_S$  by  $P_{S^2}$ , we repeated the temperature variance analysis presented in Figure 9, using  $P_{\theta^2}$  instead of  $\chi_\theta$ , and found good agreement (within a factor of 2 or less) with the original computations (Figure 12).

A third relevant assumption is that double-diffusive processes make negligible contributions to the temperature and salinity variance budgets. Stratification conditions potentially conducive to either salt fingers or diffusive convection were only observed in the WEB, associated with unstable salinity stratification indicating potential

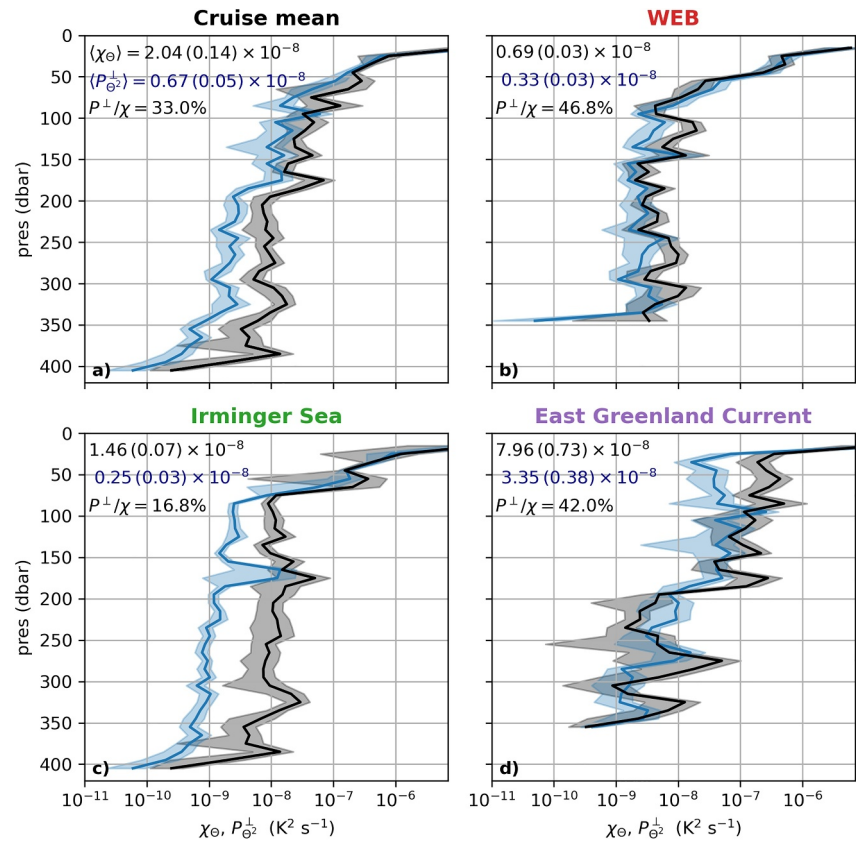


**Figure 12.** Same as Figure 9 but  $\chi_\Theta$  estimated using the Osborn and Cox (1972) formula (Equation 3) instead of direct measurements.

conditions for salt fingering instabilities (Figure 6a). However, the density ratio,  $R_\rho = (\alpha \partial \bar{\Theta} / \partial z) / (\beta \partial \bar{S}_A / \partial z)$  was systematically greater than 2 there (not shown), indicating only weak salt fingering instability, which would be easily disrupted by shear-driven turbulence (St Laurent & Schmitt, 1999). In fact, the importance of double diffusion in our observations can be generally ruled out on the grounds of the buoyancy Reynolds number and the prevailing turbulence regime, since the intermediate to energetic levels of turbulence observed throughout the cruise (Figure 11), including in areas of strong thermohaline interleaving, are likely to disrupt the development of double diffusive instabilities (St Laurent & Schmitt, 1999). This is also in line with the absence of well-defined thermohaline staircases, characteristic of double diffusion, throughout the BOCATS2 section (Figures 5a and 5b).

In addition to these assumptions, the triple decomposition approach involves selecting a method for filtering density-compensated thermohaline fine structures from the measured property profiles to obtain the background  $\Theta^m$ ,  $S_A^m$  profiles, and diagnose the rate of downscale variance transfer by microscale turbulence ( $P^\perp$ ). Due to the lack of data to obtain spatio-temporal averages, we chose to compute  $\Theta^m$  and  $S_A^m$  through a polynomial fit to the observed  $\bar{\Theta}$  and  $\bar{S}_A$  against  $\sigma_0$ . This choice entails some degree of subjectivity and uncertainty. Furthermore, by construction of the approach, any misfit between the polynomial function and the actual  $\bar{\Theta}$  and  $\bar{S}_A$  tends to be density-compensated, resulting in potential overestimation of the contribution of isopycnal stirring to mixing.

To gauge how this uncertainty may influence our conclusions, we tested an alternative method using the time-series station data set, for which we have enough data to estimate background profiles via time averaging. To obtain  $\Theta^m$  and  $S_A^m$  for each vertical cast, we first calculated time-mean  $\bar{\Theta}$  and  $\bar{S}_A$  profiles as a function of  $\sigma_0$  and then interpolated them onto the observed  $\sigma_0$  from each cast. The vertical distribution and overall magnitude of the alternative  $P^\perp$  profiles agree well with the original results, although depth-averaged  $P_{\Theta^2}^\perp$  and  $P_{S^2}^\perp$  are roughly 30%

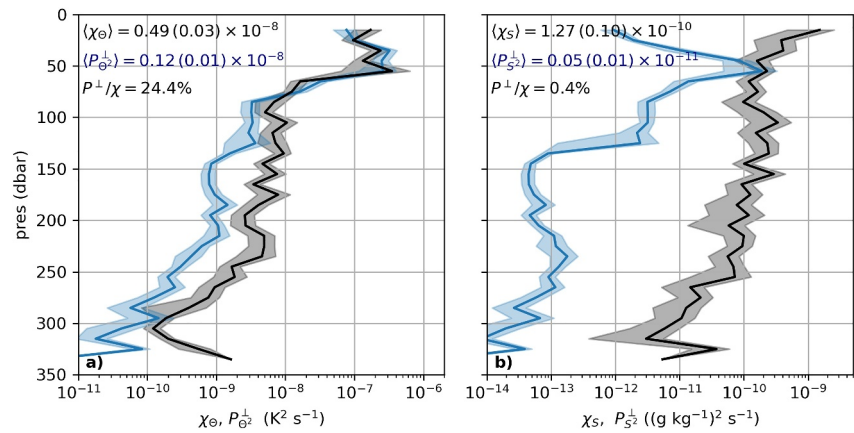


**Figure 13.** Same as Figure 8 but with an alternative computation of  $P_{\Theta}^{\perp}$  and  $P_{S_A}^{\perp}$  based on the time-mean profiles of  $\Theta$  and  $S_A$  as a function of  $\sigma_0$ .

and 70% lower, respectively (Figure 13, compared to Figure 8). This would imply a larger contribution of isopycnal stirring than originally estimated. Thus, the potential overestimation of isopycnal stirring resulting from the function misfit is not relevant here. Instead, the apparent underestimation may arise from fitting a 4-degree polynomial to more slowly varying measured  $\Theta$  and  $S_A$  profiles, yielding vertical gradients on the scale of  $\lesssim 100$  m, which may not be representative of the actual “large-scale mean”  $\Theta^m$ ,  $S_A^m$  distributions. At any rate, while there is some uncertainty associated with our calculations, the prevalence of isopycnal over diapycnal mixing emerges as a highly robust result.

#### 4.2. Temporal Variability

The main drawback of our observations and analysis is their limited spatio-temporal coverage, being restricted to the summer season of a specific year, whilst hydrographic conditions vary across a broad range of timescales in the subpolar North Atlantic, from seasonal to decadal. Such changes may modulate the magnitude and significance of mixing and its drivers. Notably, over the past 20 years, the region has experienced a cycle of cooling and freshening culminating in 2016, and subsequent warming (Desbruyères et al., 2021; Holliday et al., 2020). To ascertain to which extent these changes may have led to different mixing conditions, we analyze a microstructure data set collected in the WEB and IrmS during the OVIDE cruise 2008, prior to the onset of the freshening cycle (Figure 14).

The mean thermal and haline variance dissipation and diapycnal production profiles (Figure 14) are similar in magnitude and shape to 2023 observations (Figures 9 and 10). Depth-averaged  $\chi_\theta$  were  $0.75 \times 10^{-8} \text{ K}^2 \text{ s}^{-1}$  and  $0.72 \times 10^{-8} \text{ K}^2 \text{ s}^{-1}$  in the WEB and IrmS, respectively, with diapycnal production accounting for  $0.20 \times 10^{-8} \text{ K}^2 \text{ s}^{-1}$  and  $0.15 \times 10^{-8} \text{ K}^2 \text{ s}^{-1}$  in each case (Figures 14a and 14b). All rates are within a factor of two the 2023 observations (Figures 9b and 9c). The relative contribution of diapycnal mixing was almost identical in the IrmS at 20%, but it was lower in the WEB at 27% compared to 84% in 2023. However, the  $\chi_\theta$  and  $P_{\Theta}^{\perp}$  profiles were generally closer in value in the WEB (Figure 14a) than in the IrmS (Figure 14b), as in 2023. Depth-averaged salinity variance dissipation rates were  $3.2 \times 10^{-10} \text{ (g kg}^{-1}\text{)}^2 \text{ s}^{-1}$  and  $4.9 \times 10^{-10} \text{ (g kg}^{-1}\text{)}^2 \text{ s}^{-1}$  (Figures 14c and 14d), also very close to the 2023 values (Figures 10b and 10c). The relative contributions of diapycnal mixing to haline variance dissipation were 12% and 2.7% in the WEB and IrmS, respectively, in line with similarly low contributions of 16% and 0.6% in 2023.

Overall, the analysis of the 2008 data set suggests that our main findings hold on interannual time-scales. To gain insight into the role of seasonal variations, and further strengthen general confidence in our results, we estimated the contributions of microscale and mesoscale turbulence to mixing using an entirely independent approach based on annual-mean climatological data. We used long-term averaged temperature (and salinity) distributions from the World Ocean Atlas 2018 (Boyer et al., 2018), and global maps of diapycnal and isopycnal diffusivity from internal-wave (de Lavergne et al., 2020) and mixing-length theories (Groeskamp et al., 2020), to estimate

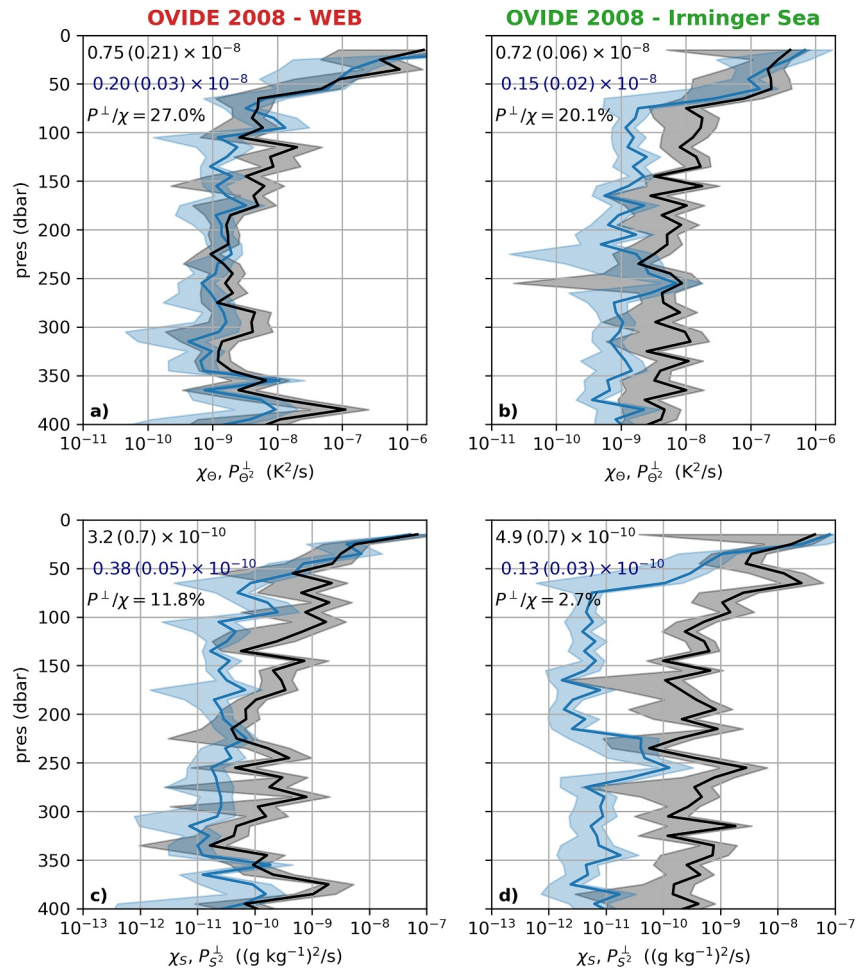


**Figure 14.** Mixing rates during the OVIDE cruise 2008. Mean profiles of the rates of thermal (a, b) and haline (c, d) variance dissipation ( $\chi$ , black), along with small-scale variance production by microscale turbulence ( $P^\perp$ , blue) in the Western European Basin (a, c) and the Irminger Sea (b, d) during the OVIDE cruise 2008.

diapycnal and isopycnal thermal (and haline) variance production rates. These terms were calculated as  $P_{\Theta^2}^\perp = 2K_\rho(\nabla_\perp\Theta^m)^2$ , and  $P_{\Theta^2}^\parallel = 2K_\parallel(\nabla_\parallel\Theta^m)^2$ , respectively, where  $K_\parallel$  is the isopycnal diffusivity from Groeskamp et al. (2020) and  $K_\rho$  is the diapycnal diffusivity from de Lavergne et al. (2020). The diapycnal ( $\nabla_\perp$ ) and isopycnal ( $\nabla_\parallel$ ) tracer gradients were estimated after mapping  $\Theta$  (and  $S_A$ ) onto neutral density coordinates. Following Equation 4, we estimated thermal variance dissipation as  $\chi_\Theta = P_{\Theta^2}^\perp + P_{\Theta^2}^\parallel$ , and equivalently for salinity. The different mixing rate profiles were interpolated from the climatology grid onto the locations of the BOCATS2 cruise stations.

Climatological mixing rates are included in Figures 9b, 9c, 10b, and 10c, with black dots showing total mixing (diapycnal plus isopycnal, that is,  $\chi = P^\perp + P^\parallel$ ) and blue dots showing diapycnal variance production ( $P^\perp$ ). The climatological estimates compare well with observations, in terms of both the mixing rates' absolute values and the relative contributions of diapycnal and isopycnal processes (Figures 9 and 10). They are compatible with an important role of isopycnal stirring in the mixing of heat and, more substantially, salt in the IrmS (Figures 9c and 10c); and a more notable contribution of diapycnal processes to thermal mixing in the WEB (Figure 9b). Comparison in the EGC was not possible due to the lack of climatological data in this shallower region. The climatological estimates thus broadly align with our observational results, and lend additional support to their relevance beyond the summer season of 2023.

## 5. Discussion

In our study, we leveraged a set of summertime microstructure observations in the eSPNA to assess the rates of variance dissipation by microscale diapycnal mixing and mesoscale isopycnal stirring, respectively. While employing microstructure observations for investigating diapycnal mixing is a well-established technique in modern oceanography (Waterhouse et al., 2014), the quantification of isopycnal stirring using this approach remains relatively underexplored, with only a few notable exceptions (Ferrari & Polzin, 2005; Naveira Garabato et al., 2016; Orúe-Echevarría et al., 2023). Building upon this work, we base our analysis on a triple decomposition of the tracer variance conservation equation, along with measurements of  $\epsilon$  and  $\chi_\theta$ . Additionally, we extend previous efforts by applying the triple decomposition to the salinity variance budget, by using the Osborn and Cox (1972) equation to estimate  $\chi_S$ .

Our analysis unveiled the dominance of mesoscale stirring in driving mixing of heat and, more importantly, salt across central water and SPMW layers of the upper eSPNA. These findings align with previous results derived from reanalysis and modeling data sets (Tooth et al., 2023; Xu et al., 2018), which emphasize the role of lateral mixing along the inter-gyre boundary and Polar Front in transforming central waters into SPMW, a key component of the AMOC (Berglund et al., 2023; Evans et al., 2023). Our measurements further indicate that the dominance of mesoscale processes is widespread, particularly in the Irminger Sea, extending beyond frontal regions. The highest rates of energy and variance dissipation were measured at the EGC, in line with previous observations (Lauderdale et al., 2008). Despite intense microscale turbulence there, isopycnal stirring was also the main driver of mixing at the EGC, accounting for >50% of heat and salt variance dissipation. This finding is consistent with vigorous isopycnal property exchanges between the ventilated basin interior and boundary currents, demonstrated in idealized and realistic simulations, as well as observations (Brüggemann & Katsman, 2019; Le Bras et al., 2020; Mackay et al., 2020; Straneo, 2006). Such exchange is considered a critical element of the AMOC.

Our findings are therefore qualitatively in accord with an important role of isopycnal stirring in the AMOC. A more quantitative measure of the significance of this role can be drawn directly from our observations. A time-scale for salinity homogenisation by isopycnal stirring can be derived from the large-scale salinity variance over the eSPNA on a representative isopycnal (e.g., a standard deviation of  $\text{std}(S_A) = 0.3 - 0.5 \text{ g kg}^{-1}$  at  $\sigma_0 = 27.4 \text{ kg m}^{-3}$ , Figure 1), and the regional-mean salinity variance dissipation due to isopycnal stirring ( $\sim 5.3 \times 10^{-10} \text{ (g kg}^{-1})^2 \text{ s}^{-1}$ , Figure 10a). The resulting time-scale ( $\tau = \text{std}(S_A)^2 / \chi_S$ ) is in the range of 5–15 years. If such time-scale is representative of the upper ocean volume (depths of  $h < 500 \text{ m}$ ) over the surface area of the eSPNA between the BOCATS2 section and the Greenland-Iceland-Scotland ridge ( $A \approx 3.8 \times 10^{12} \text{ m}^2$ ), isopycnal mixing could be responsible for  $A h / \tau = 4 - 11 \text{ Sv}$  ( $1 \text{ Sv} = 10^6 \text{ m}^3 \text{ s}^{-1}$ ) of diahaline overturning.

These isopycnal transformations are smaller, but comparable to the mean diapycnal overturning circulation in the region (10–20 Sv, Lherminier et al. (2010); Lozier et al. (2019)), and consistent with the rates of formation of SPMW (García-Ibáñez et al., 2015; Stendardo et al., 2024). This simple analysis thus suggests that diahaline transformation by isopycnal stirring may be an important process in the formation of SPMW and, by extension, the AMOC. A drawback of this estimate is that our measurements have limited spatio-temporal coverage. A full assessment of the role of mixing in the AMOC's mean state and variability would require extensive microstructure observations across the subpolar gyre to resolve the range of spatio-temporal variability of mixing in the region.

Apart from the general dominance of isopycnal stirring, we observed substantial tracer-dependent regional variations in the relative importance of diapycnal and isopycnal processes across the eSPNA. These regional patterns appear to be primarily driven by the degree of co-variability between large-scale tracer and density distributions. In regions where the considered tracer is the primary driver of vertical density stratification, and thus highly correlated with density, diapycnal mixing plays a more prominent role. For instance, thermal mixing is predominantly diapycnal in the thermally stratified WEB, and isopycnal in the EGC's halocline, where diapycnal mixing makes the largest contribution to salinity variance dissipation. In the Irminger Sea, where vertical density stratification is relatively weak, mixing is facilitated by the existence of thermohaline gradients on isopycnal surfaces, maintained by air-sea fluxes and the confluence of water masses from the northern (Arctic, Nordic Seas) and southern (subtropical) latitudes (Evans et al., 2023), leading to a dominant role of mesoscale turbulence. This dominance is more pronounced for salinity, which exhibits small diapycnal gradients.



The prevalence of diapycnal temperature mixing in the subtropically influenced WEB aligns with the temperature variance budget of the subtropical thermocline at the North Atlantic Tracer Release Experiment (NATRE) site (25°N, 30°W) (Ferrari & Polzin, 2005). In contrast to temperature, salinity mixing in the WEB is governed by isopycnal stirring. It is possible that the substantial role of isopycnal stirring is specific to the WEB's location at the boundary between the subtropical and subpolar gyres, where strong gradients exist along isopycnals, rather than representing a general characteristic of the subtropical thermocline. The WEB is the region of largest eddy kinetic energy in our sampling section (Figure 1b), possibly contributing to the importance of eddy stirring there. However, strong isopycnal property gradients and evidence for isopycnal ventilation in the lower subtropical thermocline were also reported further south in the Azores region (Robbins et al., 2000).

The importance of isopycnal stirring in the SPMW layers of the Irminger Sea is consistent with thermal variance budget analyses in intermediate and deep waters of the Drake Passage and the Malvinas Confluence in the Southern Ocean (Naveira Garabato et al., 2016; Orúe-Echevarría et al., 2023). Our results endorse the hypothesis that properties in water masses outcropping at high latitudes are preferentially mixed along isopycnals (Naveira Garabato et al., 2017), while diapycnal mixing would be more important in the subtropical thermocline. It also emerges clearly that the relative importance of either process is strongly tracer-dependent, as well as region-dependent, yet current knowledge about this variability remains limited. A large-scale investigation of the relative importance of isopycnal stirring and diapycnal mixing would enhance our understanding of how heat and chemicals are redistributed within the ocean.

## 6. Conclusions

Using microstructure observations and a small-scale tracer variance conservation framework, our study has demonstrated that isopycnal stirring by mesoscale turbulence is the primary driver of heat and salt mixing in the upper eastern subpolar North Atlantic. Our findings are consistent with an important role of mixing in the formation of subpolar mode waters from central waters, which contributes to the AMOC, and emphasize the strong isopycnal nature of these transformations, a facet often overlooked in the conventional perception of the AMOC as a primarily diapycnal phenomenon.

Isopycnal stirring emerges as a particularly crucial mechanism for salinity mixing, with potential implications for the transport of salt to the subpolar gyre (Berglund et al., 2023), a factor directly impacting the AMOC by preconditioning the region for deep wintertime convection (Born et al., 2016; Pradal & Gnanadesikan, 2014; Warren, 1983). The assessment of mesoscale stirring's importance takes on new significance, especially in predicting how the AMOC might respond to increased freshwater input from melting ice (Ditlevsen and Ditlevsen, 2023). Despite the substantial challenge of quantifying isopycnal stirring from oceanographic observations (Abernathey et al., 2022), the application of the variance budget method considered here, along with the deployment of autonomous platforms like profiling floats equipped with turbulence sensors (Roemmich et al., 2019), offers a promising avenue for addressing this challenge and advancing our comprehension of the climatic role of ocean mixing.

Further, our extension of the small-scale variance budget method to tracers beyond temperature has unveiled the tracer-dependent nature of the relative significance of isopycnal stirring. This point is particularly relevant for tracers whose large-scale distribution is uncoupled from density, such as salinity in a temperature-stratified ocean and temperature in a salinity-stratified ocean. The decoupling from density becomes more significant for tracers with biological sources or sinks, underscoring the central role of isopycnal stirring in the ocean's biogeochemical cycles (Abernathey & Ferreira, 2015; Bahl et al., 2019; Eden & Greatbatch, 2009; Spingys et al., 2021). Investigating this phenomenon could be pursued by applying the variance budget method to data from an expanding fleet of biogeochemical Argo floats (Bittig et al., 2019; Roemmich et al., 2019), in conjunction with direct or indirect estimates of diapycnal mixing rates (Whalen et al., 2012).

## Data Availability Statement

Hydrographic and microstructure data collected during the BOCATS2 cruise are available at SEANOE (Lherminier et al., 2023), associated resources can be found at UTM Data Centre (<https://doi.org/10.20351/29SG20230608>). The scripts used to process microstructure data and Jupyter notebooks used to produce the figures in the manuscript are available at ZENODO (Fernández Castro, 2024).

**Acknowledgments**

This research was supported by BOCATS2 (PID2019-104279GB-C21) project funded by MCIN/AEI/10.13039/501100011033 and by EuroGO-SHIP project (Horizon Europe #101094690). BFC is supported by NERC grants NE/W009528/1 and NE/Y002709/1. MF was funded by Juan de La Cierva Formación (FJC2019-038970-I, Ministerio de Ciencia e Innovación, Spanish Government). DFR was supported by a FPU predoctoral fellowship (FPU2021/04749) from the Spanish Ministerio de Universidades. We thank the crew members of the R/V Sarmiento de Gamboa and the technicians for their work at sea.

**References**

Abernathy, R., & Ferreira, D. (2015). Southern Ocean isopycnal mixing and ventilation changes driven by winds. *Geophysical Research Letters*, 42(23), 10357–10365. <https://doi.org/10.1002/2015GL066238>

Abernathy, R., Gnanadesikan, A., Pradal, M.-A., & Sundermeyer, M. A. (2022). Isopycnal mixing. In *Ocean mixing* (pp. 215–256). Elsevier. <https://doi.org/10.1016/B978-0-12-821512-8.00016-5>

Bahl, A., Gnanadesikan, A., & Pradal, M. (2019). Variations in ocean deoxygenation across Earth system models: Isolating the role of parameterized lateral mixing. *Global Biogeochemical Cycles*, 33(6), 703–724. <https://doi.org/10.1029/2018GB006121>

Bebieva, Y., & Lozier, M. S. (2023). Fresh water and atmospheric cooling control on density-compensated overturning in the Labrador Sea. *Journal of Physical Oceanography*, 53(11), 2575–2589. <https://doi.org/10.1175/JPO-D-22-0238.1>

Berglund, S., Döös, K., Groeskamp, S., & McDougall, T. (2023). North Atlantic Ocean circulation and related exchange of heat and salt between water masses. *Geophysical Research Letters*, 50(13), e2022GL100989. <https://doi.org/10.1029/2022GL100989>

Bittig, H. C., Maurer, T. L., Plant, J. N., Schmechtig, C., Wong, A. P. S., Claustre, H., et al. (2019). A BGC-argo guide: Planning, deployment, data handling and usage. *Frontiers in Marine Science*, 6, 502. <https://doi.org/10.3389/fmars.2019.00502>

Born, A., Stocker, T. F., & Sandø, A. B. (2016). Transport of salt and freshwater in the Atlantic subpolar gyre. *Ocean Dynamics*, 66(9), 1051–1064. <https://doi.org/10.1007/s10236-016-0970-y>

Boyer, T. P., Garcia, H. E., Locarnini, R. A., Zweng, M. M., Mishonov, A. V., Reagan, J. R., et al. (2018). World Ocean atlas 2018. Retrieved from <https://www.ncei.noaa.gov/archive/accession/NCEI-WOA18>

Brambilla, E., & Talley, L. D. (2008). Subpolar mode water in the Northeastern Atlantic: 1. Averaged properties and mean circulation. *Journal of Geophysical Research*, 113(C4), C04025. <https://doi.org/10.1029/2006JC004062>

Brügemann, N., & Katsman, C. A. (2019). Dynamics of downwelling in an eddying marginal sea: Contrasting the Eulerian and the isopycnal perspective. *Journal of Physical Oceanography*, 49(11), 3017–3035. <https://doi.org/10.1175/JPO-D-19-0090.1>

Daniault, N., Mercier, H., Lherminier, P., Sarafanov, A., Falina, A., Zunino, P., et al. (2016). The northern North Atlantic Ocean mean circulation in the early 21st century. *Progress in Oceanography*, 146, 142–158. <https://doi.org/10.1016/j.pocean.2016.06.007>

Davis, R. E. (1994). Diapycnal mixing in the ocean: The Osborn–cox model. *Journal of Physical Oceanography*, 24(12), 2560–2576. [https://doi.org/10.1175/1520-0485\(1994\)024<2560:DMITOT>2.0.CO;2](https://doi.org/10.1175/1520-0485(1994)024<2560:DMITOT>2.0.CO;2)

De Jong, M. F., Van Aken, H. M., Våge, K., & Pickart, R. S. (2012). Convective mixing in the central Irminger Sea: 2002–2010. *Deep Sea Research Part I: Oceanographic Research Papers*, 63, 36–51. <https://doi.org/10.1016/j.dsr.2012.01.003>

de Lavergne, C., Vic, C., Madec, G., Roquet, F., Waterhouse, A. F., Whalen, C. B., et al. (2020). A parameterization of local and remote tidal mixing. *Journal of Advances in Modeling Earth Systems*, 12(5), e2020MS002065. <https://doi.org/10.1029/2020MS002065>

Desbruyères, D., Chafik, L., & Maze, G. (2021). A shift in the ocean circulation has warmed the subpolar North Atlantic Ocean since 2016. *Communications Earth & Environment*, 2(1), 48. <https://doi.org/10.1038/s43247-021-00120-y>

Ditlevsen, P., & Ditlevsen, S. (2023). Warming of a forthcoming collapse of the Atlantic meridional overturning circulation. *Nature Communications*, 14(1), 4254. <https://doi.org/10.1038/s41467-023-39810-w>

Eden, C., & Greatbatch, R. J. (2009). A diagnosis of isopycnal mixing by mesoscale eddies. *Ocean Modelling*, 27(1–2), 98–106. <https://doi.org/10.1016/j.ocemod.2008.12.002>

Evans, D. G., Holliday, N. P., Bacon, S., & Le Bras, I. (2023). Mixing and air–sea buoyancy fluxes set the time-mean overturning circulation in the subpolar North Atlantic and Nordic Seas. *Ocean Science*, 19(3), 745–768. <https://doi.org/10.5194/os-19-745-2023>

Fernández Castro, B. (2024). Microstructure Processing Code (MSS) and Analysis notebooks—BOCATS2 cruise. *Zenodo*. <https://doi.org/10.5281/zenodo.11391699>

Fernández Castro, B., Peña, M., Nogueira, E., Gilcoto, M., Broullón, E., Comesaña, A., et al. (2022). Intense upper ocean mixing due to large aggregations of spawning fish. *Nature Geoscience*, 15(4), 287–292. <https://doi.org/10.1038/s41561-022-00916-3>

Ferrari, R., & Polzin, K. L. (2005). Finescale structure of the T–S relation in the eastern North Atlantic. *Journal of Physical Oceanography*, 35(8), 1437–1454. <https://doi.org/10.1175/JPO2763.1>

Ferron, B., Kokoszka, F., Mercier, H., & Lherminier, P. (2014). Dissipation rate estimates from microstructure and finescale internal wave observations along the A25 Greenland–Portugal OVIDE line. *Journal of Atmospheric and Oceanic Technology*, 31(11), 2530–2543. <https://doi.org/10.1175/JTECH-D-14-00036.1>

García-Ibáñez, M. I., Pardo, P. C., Carracedo, L. I., Mercier, H., Lherminier, P., Ríos, A. F., & Pérez, F. F. (2015). Structure, transports and transformations of the water masses in the Atlantic Subpolar Gyre. *Progress in Oceanography*, 135, 18–36. <https://doi.org/10.1016/j.pocean.2015.03.009>

Garrett, C. (2001). Stirring and mixing: What are the rate-controlling processes? Stirring to mixing in a stratified ocean. *Proceedings Hawaiian Winter Workshop [12th] Held in the University of Hawaii at Manoa*.

Groeskamp, S., LaCasce, J. H., McDougall, T. J., & Rogé, M. (2020). Full-depth global estimates of ocean mesoscale eddy mixing from observations and theory. *Geophysical Research Letters*, 47(18), e2020GL089425. <https://doi.org/10.1029/2020GL089425>

Holliday, N. P., Bersch, M., Bex, B., Chafik, L., Cunningham, S., Florindo-López, C., et al. (2020). Ocean circulation causes the largest freshening event for 120 years in eastern subpolar North Atlantic. *Nature Communications*, 11(1), 585. <https://doi.org/10.1038/s41467-020-14474-y>

Ijichi, T., St. Laurent, L., Polzin, K. L., & Toole, J. M. (2020). How variable is mixing efficiency in the abyss? *Geophysical Research Letters*, 47(7), e2019GL086813. <https://doi.org/10.1029/2019GL086813>

Joyce, T. M. (1977). A note on the lateral mixing of water masses. *Journal of Physical Oceanography*, 7(4), 626–629. [https://doi.org/10.1175/1520-0485\(1977\)007<0626:ANOTLM>2.0.CO;2](https://doi.org/10.1175/1520-0485(1977)007<0626:ANOTLM>2.0.CO;2)

Jurado, E., Dijkstra, H. A., & van der Woerd, H. J. (2012a). Microstructure observations during the spring 2011 STRATIPHYT-II cruise in the northeast Atlantic. *Ocean Science*, 8(6), 945–957. <https://doi.org/10.5194/os-8-945-2012>

Jurado, E., van der Woerd, H. J., & Dijkstra, H. A. (2012b). Microstructure measurements along a quasi-meridional transect in the northeastern Atlantic Ocean. *Journal of Geophysical Research*, 117(C4), C04016. <https://doi.org/10.1029/2011JC007137>

Kunze, E., Lien, R.-C., Whalen, C. B., Girton, J. B., Ma, B., & Buijsman, M. C. (2023). Seasonal variability of near-inertial/semidiurnal fluctuations and turbulence in the subarctic North Atlantic. *Journal of Physical Oceanography*, 53(12), 2717–2735. <https://doi.org/10.1175/JPO-D-22-0231.1>

Lauderdale, J. M., Bacon, S., Naveira Garabato, A. C., & Holliday, N. P. (2008). Intensified turbulent mixing in the boundary current system of southern Greenland. *Geophysical Research Letters*, 35(4), L04611. <https://doi.org/10.1029/2007GL032785>

Lazier, J., Hendry, R., Clarke, A., Yashayaev, I., & Rhines, P. (2002). Convection and restrati in the Labrador Sea. *Deep Sea Research Part I: Oceanographic Research Papers*, 49(10), 1819–1835. [https://doi.org/10.1016/S0967-0637\(02\)00064-x](https://doi.org/10.1016/S0967-0637(02)00064-x)

- Le Bras, I. A., Straneo, F., Holte, J., De Jong, M. F., & Holliday, N. P. (2020). Rapid export of waters formed by convection near the Irminger Sea's western boundary. *Geophysical Research Letters*, *47*(3), e2019GL085989. <https://doi.org/10.1029/2019GL085989>
- Lee, M.-M., Marshall, D. P., & Williams, R. G. (1997). On the eddy transfer of tracers: Advective or diffusive? *Journal of Marine Research*, *55*(3), 483–505. <https://doi.org/10.1357/0022240973224346>
- Lherminier, P., Mercier, H., Huck, T., Gourcuff, C., Perez, F. F., Morin, P., et al. (2010). The Atlantic meridional overturning circulation and the subpolar gyre observed at the A25-OVIDE section in June 2002 and 2004. *Deep-Sea Research I*, *57*(11), 1374–1391. <https://doi.org/10.1016/j.dsr.2010.07.009>
- Lherminier, P., Velo, A., Perez, F. F., Le Bihan, C., Hamon, M., Le Bot, P., et al. (2023). BOCATS2 2023 Cruise data along the A25-OVIDE section. *SEANOE*. <https://doi.org/10.17882/95607>
- Lozier, M. S., Li, F., Bacon, S., Bahr, F., Bower, A. S., Cunningham, S. A., et al. (2019). A sea change in our view of overturning in the subpolar North Atlantic. *Science*, *363*(6426), 516–521. <https://doi.org/10.1126/science.aau6592>
- Mackay, N., Wilson, C., Holliday, N. P., & Zika, J. D. (2020). The observation-based application of a regional thermohaline inverse method to diagnose the formation and transformation of water masses north of the OSNAP array from 2013 to 2015. *Journal of Physical Oceanography*, *50*(6), 1533–1555. <https://doi.org/10.1175/JPO-D-19-0188.1>
- Marsh, R. (2000). Recent variability of the North Atlantic thermohaline circulation inferred from surface heat and freshwater fluxes. *Journal of Climate*, *13*(18), 3239–3260. [https://doi.org/10.1175/1520-0442\(2000\)013\(3239:RVOTNA\)2.0.CO;2](https://doi.org/10.1175/1520-0442(2000)013(3239:RVOTNA)2.0.CO;2)
- McCartney, M. S., & Talley, L. D. (1982). The subpolar mode water of the North Atlantic ocean. *Journal of Physical Oceanography*, *12*(11), 1169–1188. [https://doi.org/10.1175/1520-0485\(1982\)012\(1169:TSMWOT\)2.0.CO;2](https://doi.org/10.1175/1520-0485(1982)012(1169:TSMWOT)2.0.CO;2)
- Naveira Garabato, A. C., MacGilchrist, G. A., Brown, P. J., Evans, D. G., Meijers, A. J. S., & Zika, J. D. (2017). High-latitude ocean ventilation and its role in Earth's climate transitions. *Philosophical Transactions of the Royal Society A: Mathematical, Physical & Engineering Sciences*, *375*(2102), 20160324. <https://doi.org/10.1098/rsta.2016.0324>
- Naveira Garabato, A. C., Polzin, K. L., Ferrari, R., Zika, J. D., & Forryan, A. (2016). A microscale view of mixing and overturning across the Antarctic circumpolar current. *Journal of Physical Oceanography*, *46*(1), 233–254. <https://doi.org/10.1175/JPO-D-15-0025.1>
- Oakey, N. S. (1982). Determination of the rate of dissipation of turbulent energy from simultaneous temperature and velocity shear microstructure measurements. *Journal of Physical Oceanography*, *12*(3), 256–271. [https://doi.org/10.1175/1520-0485\(1982\)012\(256:dotdrod\)2.0.co;2](https://doi.org/10.1175/1520-0485(1982)012(256:dotdrod)2.0.co;2)
- Orúe-Echevarría, D., Polzin, K. L., Naveira Garabato, A. C., Forryan, A., & Pelegrí, J. L. (2023). Mixing and overturning across the Brazil-Malvinas confluence. *Journal of Geophysical Research: Oceans*, *128*(5), e2022JC018730. <https://doi.org/10.1029/2022JC018730>
- Osborn, T. R. (1980). Estimates of the local rate of vertical diffusion from dissipation measurements. *Journal of Physical Oceanography*, *10*(1), 83–89. [https://doi.org/10.1175/1520-0485\(1980\)010\(0083:EOTLRO\)2.0.CO;2](https://doi.org/10.1175/1520-0485(1980)010(0083:EOTLRO)2.0.CO;2)
- Osborn, T. R., & Cox, C. S. (1972). Oceanic fine structure. *Geophysical Fluid Dynamics*, *3*(1), 321–345. <https://doi.org/10.1080/03091927208236085>
- Pérez, F. F., Mercier, H., Vázquez-Rodríguez, M., Lherminier, P., Velo, A., Pardo, P. C., et al. (2013). Atlantic Ocean CO<sub>2</sub> uptake reduced by weakening of the meridional overturning circulation. *Nature Geoscience*, *6*(2), 146–152. <https://doi.org/10.1038/ngeo1680>
- Petit, T., Lozier, M. S., Josey, S. A., & Cunningham, S. A. (2020). Atlantic deep water formation occurs primarily in the Iceland basin and Irminger Sea by local buoyancy forcing. *Geophysical Research Letters*, *47*(22), e2020GL091028. <https://doi.org/10.1029/2020GL091028>
- Piccolroaz, S., Fernández-Castro, B., Toffolon, M., & Dijkstra, H. A. (2021). A multi-site, year-round turbulence microstructure atlas for the deep perialpine Lake Garda. *Scientific Data*, *8*(1), 188. <https://doi.org/10.1038/s41597-021-00965-0>
- Pickart, R. S., Straneo, F., & Moore, G. W. K. (2003). Is Labrador Sea water formed in the Irminger basin? *Deep-Sea Research I*, *50*(1), 23–52. [https://doi.org/10.1016/S0967-0637\(02\)00134-6](https://doi.org/10.1016/S0967-0637(02)00134-6)
- Pradal, M.-A., & Gnanadesikan, A. (2014). How does the Redi parameter for mesoscale mixing impact global climate in an Earth System Model? *Journal of Advances in Modeling Earth Systems*, *6*(3), 586–601. <https://doi.org/10.1002/2013MS000273>
- Prandke, H., & Stips, A. (1998). Test measurements with an operational microstructure-turbulence profiler: Detection limit of dissipation rates. *Aquatic Science*, *60*(3), 191–209. <https://doi.org/10.1007/s000270050036>
- Robbins, P. E., Price, J. F., Owens, W. B., & Jenkins, W. J. (2000). The importance of lateral diffusion for the ventilation of the lower thermocline in the subtropical North Atlantic. *Journal of Physical Oceanography*, *30*(1), 67–89. [https://doi.org/10.1175/1520-0485\(2000\)030\(0067:tioldf\)2.0.co;2](https://doi.org/10.1175/1520-0485(2000)030(0067:tioldf)2.0.co;2)
- Roemmich, D., Alford, M. H., Claustre, H., Johnson, K., King, B., Moum, J., et al. (2019). On the future of Argo: A global, full-depth, multi-disciplinary array. *Frontiers in Marine Science*, *6*, 439. <https://doi.org/10.3389/fmars.2019.00439>
- Spingys, C. P., Williams, R. G., Tuerena, R. E., Naveira Garabato, A., Vic, C., Forryan, A., & Sharples, J. (2021). Observations of nutrient supply by mesoscale eddy stirring and small-scale turbulence in the oligotrophic North Atlantic. *Global Biogeochemical Cycles*, *35*(12), e2021GB007200. <https://doi.org/10.1029/2021GB007200>
- Stendardo, I., Buongiorno Nardelli, B., Durante, S., Iudicone, D., & Kieke, D. (2024). Interannual variability of subpolar mode water in the Subpolar North Atlantic. *Journal of Geophysical Research: Oceans*, *129*(3), e2023JC019937. <https://doi.org/10.1029/2023JC019937>
- St Laurent, O., & Schmitt, R. W. (1999). The contribution of salt fingers to vertical mixing in the North Atlantic tracer Release experiment. *Journal of Physical Oceanography*, *29*(7), 1404–1424. [https://doi.org/10.1175/1520-0485\(1999\)029\(1404:TCOSFT\)2.0.CO;2](https://doi.org/10.1175/1520-0485(1999)029(1404:TCOSFT)2.0.CO;2)
- Straneo, F. (2006). On the connection between dense water formation, overturning, and poleward heat transport in a convective basin. *Journal of Physical Oceanography*, *36*(9), 1822–1840. <https://doi.org/10.1175/JPO2932.1>
- Tooth, O. J., Johnson, H. L., Wilson, C., & Evans, D. G. (2023). Seasonal overturning variability in the eastern North Atlantic subpolar gyre: A Lagrangian perspective. *Ocean Science*, *19*(3), 769–791. <https://doi.org/10.5194/os-19-769-2023>
- Warren, B. A. (1983). Why is no deep water formed in the North Pacific? *Journal of Marine Research*, *41*(2), 327–347. <https://doi.org/10.1357/002224083788520207>
- Waterhouse, A. F., MacKinnon, J. A., Nash, J. D., Alford, M. H., Kunze, E., Simmons, H. L., et al. (2014). Global patterns of Diapycnal mixing from measurements of the turbulent dissipation rate. *Journal of Physical Oceanography*, *44*(7), 1854–1872. <https://doi.org/10.1175/JPO-D-13-0104.1>
- Whalen, C. B., Talley, L. D., & MacKinnon, J. A. (2012). Spatial and temporal variability of global ocean mixing inferred from Argo profiles. *Geophysical Research Letters*, *39*(18), L18612. <https://doi.org/10.1029/2012GL053196>
- Xu, X., Rhines, P. B., & Chassignet, E. P. (2018). On mapping the Diapycnal water mass transformation of the upper North Atlantic ocean. *Journal of Physical Oceanography*, *48*(10), 2233–2258. <https://doi.org/10.1175/JPO-D-17-0223.1>
- Yeager, S., Castruccio, F., Chang, P., Danabasoglu, G., Maroon, E., Small, J., et al. (2021). An outsized role for the Labrador Sea in the multidecadal variability of the Atlantic overturning circulation. *Science Advances*, *7*(41), eabh3592. <https://doi.org/10.1126/sciadv.abh3592>
- Zou, S., Lozier, M. S., Li, F., Abernathy, R., & Jackson, L. (2020). Density-compensated overturning in the Labrador Sea. *Nature Geoscience*, *13*(2), 121–126. <https://doi.org/10.1038/s41561-019-0517-1>